The Astrophysical Journal, 721:1090–1104, 2010 October 1 doi:10.1088/0004-637X/721/2/1090

UNUSUAL PAH EMISSION IN NEARBY EARLY-TYPE GALAXIES: A SIGNATURE OF AN INTERMEDIATE-AGE STELLAR POPULATION?

O. Vega[1], A. Bressan[1,2,3], P. Panuzzo[4], R. Rampazzo[2], M. Clemens[2], G. L. Granato[5], L. Buson[2], L. Silva[5], and W. W. Zeilinger[6]

[1] Instituto Nacional de Astrofísica, Optica y Electrónica, Apdos. Postales 51 y 216, C.P. 72000 Puebla, Pue., Mexico; ovega@inaoep.mx
[2] INAF Osservatorio Astronomico di Padova, vicolo dell'Osservatorio 5, 35122 Padova, Italy
[3] Scuola Internazionale Superiore de Studi Avanzati (SISSA), via Beirut 4, 34014 Trieste, Italy
[4] CEA, Laboratoire AIM, Irfu/SAp, Orme des Merisiers, F-91191 Gif-sur-Yvette, France
[5] INAF, Osservatorio Astronomico di Trieste, Via Tiepolo 11, I-34131 Trieste, Italy
[6] Institut fur Astronomie, Universitat Wien, Turkenschanzstrasse 17, A-1180 Wien, Austria
Received 2009 February 7; accepted 2010 August 2; published 2010 September 7

ABSTRACT

We present the analysis of *Spitzer*–IRS spectra of four early-type galaxies (ETGs), NGC 1297, NGC 5044, NGC 6868, and NGC 7079, all classified as LINERs in the optical bands. Their IRS spectra present the full series of H_2 rotational emission lines in the range 5–38 μm, atomic lines, and prominent polycyclic aromatic hydrocarbon (PAH) features. We investigate the nature and origin of the PAH emission, characterized by unusually low 6–9/11.3 μm interband ratios. After the subtraction of a passive ETG template, we find that the 7–9 μm spectral region requires dust features not normally present in star-forming galaxies. Each spectrum is then analyzed with the aim of identifying their components and origin. In contrast to normal star-forming galaxies, where cationic PAH emission prevails, our 6–14 μm spectra seem to be dominated by large and neutral PAH emission, responsible for the low 6–9/11.3 μm ratios, plus two broad dust emission features peaking at 8.2 μm and 12 μm. These broad components, observed until now mainly in evolved carbon stars and usually attributed to pristine material, contribute approximately 30%–50% of the total PAH flux in the 6–14 μm region. We propose that the PAH molecules in our ETGs arise from fresh carbonaceous material that is continuously released by a population of carbon stars, formed in a rejuvenation episode that occurred within the last few Gyr. The analysis of the MIR spectra allows us to infer that, in order to maintain the peculiar size and charge distributions biased to large and neutral PAHs, this material must be shocked and excited by the weak UV interstellar radiation field of our ETGs.

Key words: galaxies: elliptical and lenticular, cD – galaxies: evolution – galaxies: individual (NGC 1297, NGC 5044, NGC 6868) – galaxies: stellar content

Online-only material: color figures

1. INTRODUCTION

The understanding of the evolution of early-type galaxies (i.e., E and S0 galaxies) has been greatly enhanced by the study of their interstellar medium (ISM; see, e.g., Renzini 2007, for a review). This component and its relevance in early-type galaxies (ETGs, hereafter) were widely neglected in early studies, since these galaxies were, for a long time, considered to be essentially devoid of interstellar gas and dust. In the last two decades, however, multiwavelength observations have changed this picture and have detected the presence of a multiphase ISM (e.g., Bregman et al. 1992; Bettoni et al. 2001; Boselli et al. 2005; Morganti et al. 2006). The bulk of the gas in ellipticals is heated to the virial temperature, emitting in X-rays (e.g., Bregman et al. 1992). Some ETGs also contain large dust masses, which is surprising given the efficiency of sputtering by their hot plasma (e.g., Knapp et al. 1989; Ferrari et al. 1999; Temi et al. 2004; Clemens et al. 2010). Even more surprising was the detection of polycyclic aromatic hydrocarbons (PAHs) in ETG spectra (e.g., Xilouris et al. 2004; Kaneda et al. 2005, 2008; Bressan et al. 2006b; Panuzzo et al. 2007; Bregman et al. 2008) because dust molecules as small as PAHs are expected to be more easily destroyed by interaction with hot plasma (e.g., Dwek & Arendt 1992).

PAH emission is a typical feature of the mid-infrared (hereafter MIR) spectra of star-forming galaxies (e.g., Roussel et al. 2001; Förster Schreiber et al. 2004; Peeters et al. 2004; Vega et al. 2005), which are dominated by the strong 6.2, 7.7, and 8.6 μm emission bands usually attributed to the C–C stretching and C–H in-plane bending modes of ionized PAHs (see Tielens 2008 and references therein). However, the PAH spectra of ETGs are often different from those of star-forming galaxies. The most striking characteristic is the unusual PAH inter-band emission ratio between the 7.7 μm complex and the 11.3 μm complex (Kaneda et al. 2005; Bressan et al. 2006b). So, while in star-forming galaxies the 6.2, 7.7, and 8.6 μm features dominate the PAH spectrum, they are very weak in these ETGs, in spite of a strong 11.3 μm band.

There already exist studies in the literature aimed at understanding the nature and origin of these PAH emission features, as well as the physical conditions of the ISM that allow the survival of this material in the observed ratios. Smith et al. (2007), analyzing the SINGS galaxies sample, found that some LINERs also have unusual PAH ratios. They suggest that these ratios could be due to the relatively hard radiation field from a low-luminosity active galactic nucleus (AGN), which modifies the emitting grain distribution at the expense of the smaller PAHs. Bregman et al. (2008) claim that once the continuum of the underlying stellar population, which has a broad dip just below the 7.7 μm complex, is properly subtracted, the low 7.7–11.3 μm ratio turns into a value typical of the ISM of late-type galaxies. In contrast, Kaneda et al. (2008) have shown cases where these ratios remain anomalous even after the proper removal of the underlying stellar population. These authors

conclude that the anomalous ratios are likely due to the presence of a larger fraction of neutral PAHs with respect to ionized PAHs, contrary to what happens in the ISM of late-type galaxies. They ascribe this anomalous mixture to recent accretion events.

In this paper, we deepen the investigation of this problem by presenting a new approach to the study of these peculiar ETGs. We analyze our high signal-to-noise ratio (S/N) *Spitzer*–IRS observations of four ETGs (see Table A.1 in the Appendix for the galaxy classification) in low density environments (LDEs), namely, NGC 1297, NGC 5044, NGC 6868, and NGC 7079, which display "unusual" PAH emission in their MIR spectra. For our study, we make use of theoretical spectra and empirical dust feature templates recently reported in the literature (see, e.g., Rapacioli et al. 2005; Berné et al. 2007; Joblin et al. 2008; Bauschlicher et al. 2008; Joblin et al. 2009; Berné et al. 2009). This method has the advantage of isolating the components responsible for the emission, thus providing more insight into the origin and evolution of this ISM component (Allamandola et al. 1999). We advance a new scenario, where this PAH emission is naturally explained in terms of the presence of an underlying intermediate-age population of carbon stars, which are continuously feeding the ISM with pristine carbonaceous material. If our interpretation is correct, the anomalous PAH spectra are strong evidence of a rejuvenation episode that affected the evolution of the ETGs in the recent past.

The paper is organized as follows. In Section 2, we provide the details of the observations and data reduction methods. In Section 3, we measure and provide detailed information for each single PAH emission feature observed in the spectra and for PAH inter-band ratios. This information is used to compare our spectra with existing classifications. In Section 4, we explore the nature of the PAH carriers by using component templates available both from observations and theory. This method allows us to identify families of emitters typical of different environments. In Section 5, we analyze the MIR emission lines sensitive to the physical conditions of the medium giving place to the PAH emission. In Section 6, we discuss our results and compare them with other studies. The relevant properties of our ETGs, as known so far, are provided in the Appendix.

2. MID-INFRARED OBSERVATIONS AND DATA REDUCTION

Spitzer–IRS spectral observations of all galaxies were obtained during the third *Spitzer* General Observer Cycle 3 on 2007 June 1 as part of program ID 30256 (PI: R. Rampazzo).

The observations were performed in Standard Staring mode with low-resolution ($R \sim 64$–128) modules SL1 (7.4–14.5 μm), SL2 (5–8.7 μm), LL2 (14.1–21.3 μm), and LL1 (19.5–38 μm). Exposure times for each galaxy are given in Table 1.

We have devised an ad hoc procedure to flux-calibrate the spectra that exploit the large degree of symmetry that characterizes the light distribution in early-type galaxies. The reduction procedure is fully described in Bressan et al. (2006b); here we only summarize the main steps.

For SL (short-low module; 5–15 μm) observations, the sky background was removed by subtracting observations taken in different orders, but at the same nod position. LL (long-low module; 15–37 μm) segments were sky-subtracted by differencing the two nod positions.

We obtained new e^- s^{-1} to Jy flux conversions by applying a correction for aperture losses (ALCF) and a correction for slit losses (SLCF) to the flux conversion tables provided by the Spitzer Science Center (e.g., Kennicutt et al. 2003). By applying the ALCF and SLCF corrections we obtained the flux received by the slit.

Table 1
IRS Observations

Galaxy IRS Module	Ramp Duration (s)	Number of Cycles	AOR Key
NGC 1297			17923584
SL1	60	19	
SL2	60	19	
LL2	120	14	
LL1	120	8	
NGC 5044			17926144
SL1	60	19	
SL2	60	19	
LL2	120	14	
LL1	120	8	
NGC 6868			17926912
SL1	60	6	
SL2	60	6	
LL2	120	13	
LL1	120	8	
NGC 7079			17927168
SL1	60	19	
SL2	60	19	
LL2	120	14	
LL1	120	8	

For each galaxy, we then simulated the corresponding observed profile along the slits by convolving a wavelength-dependent bidimensional intrinsic surface brightness profile with the instrumental point-spread function (PSF). The adopted profile was a two-dimensional modified King law (Elson et al. 1987). By fitting the observed profiles with the simulated ones, we could reconstruct the intrinsic profiles and the corresponding intrinsic spectral energy distribution (SED). This procedure allowed us to determine whether a particular feature was spatially extended or not.

Finally, the spectrum was extracted in a fixed width (18″ for SL and 10.″2 for LL) around the maximum intensity. After normalization to the same area (3.″6 × 18″) there remain differences between the SL and LL spectral segments between 3% (NGC 5044) and 14% (NGC 6868). In order to account for these differences, the LL spectrum has been rescaled to match the SL one in the common wavelengths.

The uncertainty on the flux was evaluated by considering two sources of noise: the instrumental plus background noise and the Poissonian noise of the source. The former was evaluated by measuring the variance of pixel values in background-subtracted, co-added images far from the source. The Poissonian noise of the sources was estimated as the square root of the ratio between the variance of the number of e^- extracted per pixel in each exposure, and the number of the exposures. The total noise was obtained by summing the two sources in quadrature and by multiplying by the square root of the extraction width in pixels. We note that the overall absolute photometric uncertainty of IRS is 10%, while the slope deviation within a single segment (affecting all spectra in the same way) is less than 3% (see the Spitzer Observers Manual).

The flux-calibrated de-redshifted IRS spectra of NGC 1297, NGC 5044, NGC 6868, and NCG 7079 are shown in Figure 1. In the same figure, we also plot, for comparison, the spectra of an ETG which has experienced a recent episode of star formation, NGC 4435 (Panuzzo et al. 2007), and of two typical passively evolving ETGs, the cluster ETG NGC 4621 (see Bressan et al.

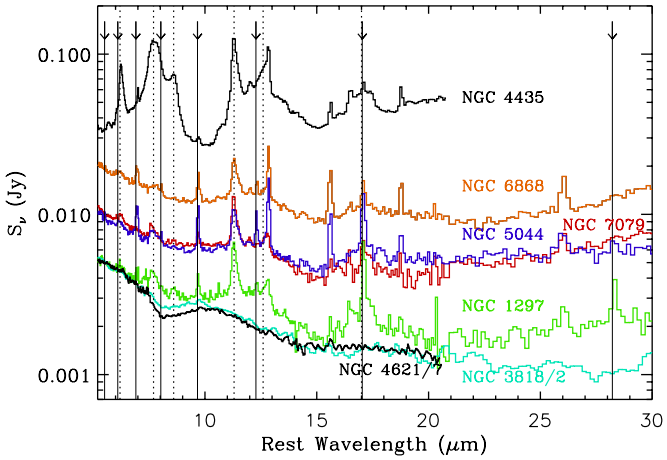

Figure 1. *Spitzer*–IRS spectra of NGC 1297, NGC 5044, NGC 6868, and NGC 7079. Dotted lines indicate the positions of the most relevant PAH complexes at 6.2 μm, 7.7 μm, 8.6 μm, 11.3 μm, 12.7 μm, and 17 μm. Arrows and thin solid lines indicate the positions of the H_2 rotational lines. For comparison, we also show the spectra of an ETG with a recent burst of star formation (NGC 4435; Panuzzo et al. 2007) and of two passively evolving ETGs: the cluster ETG, NGC 4621 (Bressan et al. 2006a), and the field ETG, NGC 3818 (Panuzzo et al. 2010), both scaled to the flux of NGC 1297 at 5.6 μm.

(A color version of this figure is available in the online journal.)

2006b) and the field ETG NGC 3818 (Panuzzo et al. 2010). In spite of the similarity to the passive galaxies, especially in the lower wavelength spectral range, the IRS spectra of our objects show several signatures of activity, such as (1) strong PAH emission at $\lambda_0 \sim 11.3\,\mu$m, similar to that found by Kaneda et al. (2005) in four ETGs and the well-developed complex of PAH emission near 17 μm; (2) other weak dust features at 6.2 μm, 7.7 μm, 8.6 μm, and 12.7 μm, usually attributed to PAH molecules (e.g., Allamandola et al. 1989; Puget & Leger 1989; Tielens 2008); (3) strikingly strong emission of pure H_2 rotational lines; (4) forbidden nebular emission lines of Ar, Fe, Ne, O, S, and Si; and (5) warm dust continuum emission.

3. ANALYSIS OF THE PAH EMISSION FEATURES

3.1. Removal of the Underlying Stellar and Dust Continua

In order to study the PAH features it is necessary to properly remove the underlying stellar and dust continua from each spectrum.

We adopt a semi-empirical, high S/N, template derived from the analysis of passive ETGs to describe the stellar continuum representative of the old stellar population. That template was built averaging the NIR (J-H-K Two- Micron All-Sky Survey, 2MASS) data and the 5–40 μm IRS–*Spitzer* spectra of three passively evolving ETGs in low-density environments, namely, NGC 1389, NGC 1426, and NGC 3818 (Panuzzo et al. 2010). The stellar continuum template shows the dip at 8 μm likely due to photospheric SiO absorption bands (e.g., Verhoelst et al. 2009) and the bump of silicate emission at $\approx$10 μm likely due to dusty circumstellar O-rich asymptotic giant branch (AGB) star envelopes. Both are features typical of passively evolving ETGs (Bressan et al. 1998, 2006b). In Figure 1, as an example, we illustrate the range of variation of these stellar features in the stellar continuum of NGC 4621 and NGC 3818 located in Virgo and in the field, respectively.

In order to properly remove the underlying continuum from the IRS spectra, we use the 2MASS magnitudes within an aperture of 5″ radius, which is close to that of our IRS spectra

Table 2
2MASS Magnitudes within the Central 5 arcsec Radius

Name	*J*	*H*	*K*
NGC 1297	11.98 ± 0.01	11.24 ± 0.01	11.01 ± 0.01
NGC 5044	11.24 ± 0.01	10.51 ± 0.01	10.22 ± 0.01
NGC 6868	10.41 ± 0.01	9.67 ± 0.01	9.40 ± 0.01
NGC 7079	11.10 ± 0.01	10.41 ± 0.01	10.17 ± 0.01

(Panuzzo et al. 2007). The NIR magnitudes and errors are listed in Table 2. Assuming that the NIR fluxes are completely due to the stellar component, we normalize our stellar continuum template to the observed flux in the *H* band, and calculate the contribution of the stellar continuum to the MIR spectra. We find that the old stellar population contributes about 97.5%, 98.5%, 99.6%, and 98.5% of the observed fluxes at 5.6 μm for NGC 1297, NGC 5044, NGC 6868, and NGC 7079, respectively. We then may consider that the old stellar population dominates the MIR emission at shorter wavelengths. This was already expected from the comparison with passive ETGs shown in Figure 1. However, this is not always the case. Indeed Panuzzo et al. (2007) found that the contribution of the stellar component to the MIR emission of NGC 4435 was less than 30% at 5.6 μm.

After a proper subtraction of the stellar continuum, the galaxies show a residual continuum component due to dust emission. It is removed by fitting up to five modified blackbodies, with temperatures ranging from 20 to 350 K. Note that these dust components are chosen just to smoothly reproduce a realistic underlying dust continuum without any attempt to provide a physical interpretation.

The whole process of continuum subtraction and the final results are shown in Figure 2. The final spectra are a combination of emission lines and dust features.

All the spectra, normalized to the peak of the 11.3 μm feature, are shown in Figure 3. For comparison, in the same figure we also plot the spectrum of NGC 1482, a H II galaxy with PAH emission typical of a star-forming galaxy (Smith et al. 2007).

3.2. Analysis of the Dust Feature Emission

Before discussing the individual PAH features, we point out the following points on the general shape of the spectra.

1. The continuum-subtracted spectra of our ETG sample are very similar. At the same time, in the 5–9 μm spectral range, they significantly differ from star-forming galaxies, represented by NGC 1482.
2. A broad 7.7 μm feature, hardly recognizable in the original spectra, appears after continuum subtraction because of the presence of the dip at 8 μm in the underlying stellar continuum.
3. The PAH bands at 8.6, 7.7, and primarily at 6.2 μm are much less intense than those observed in the integrated spectrum of star-forming galaxies (see the NGC 1482 spectrum). On the contrary, the emission at 17 μm looks very similar to that of star-forming galaxies.
4. The positions of the peak of the 7.7 μm band in NGC 6868 and in NGC 5044 are shifted to longer wavelengths.
5. Despite the similarity of the PAH emission bands in the four ETGs, the emission lines show considerable variation from galaxy to galaxy. These emission lines will be analyzed for a larger sample in a companion paper (Panuzzo et al. 2010).

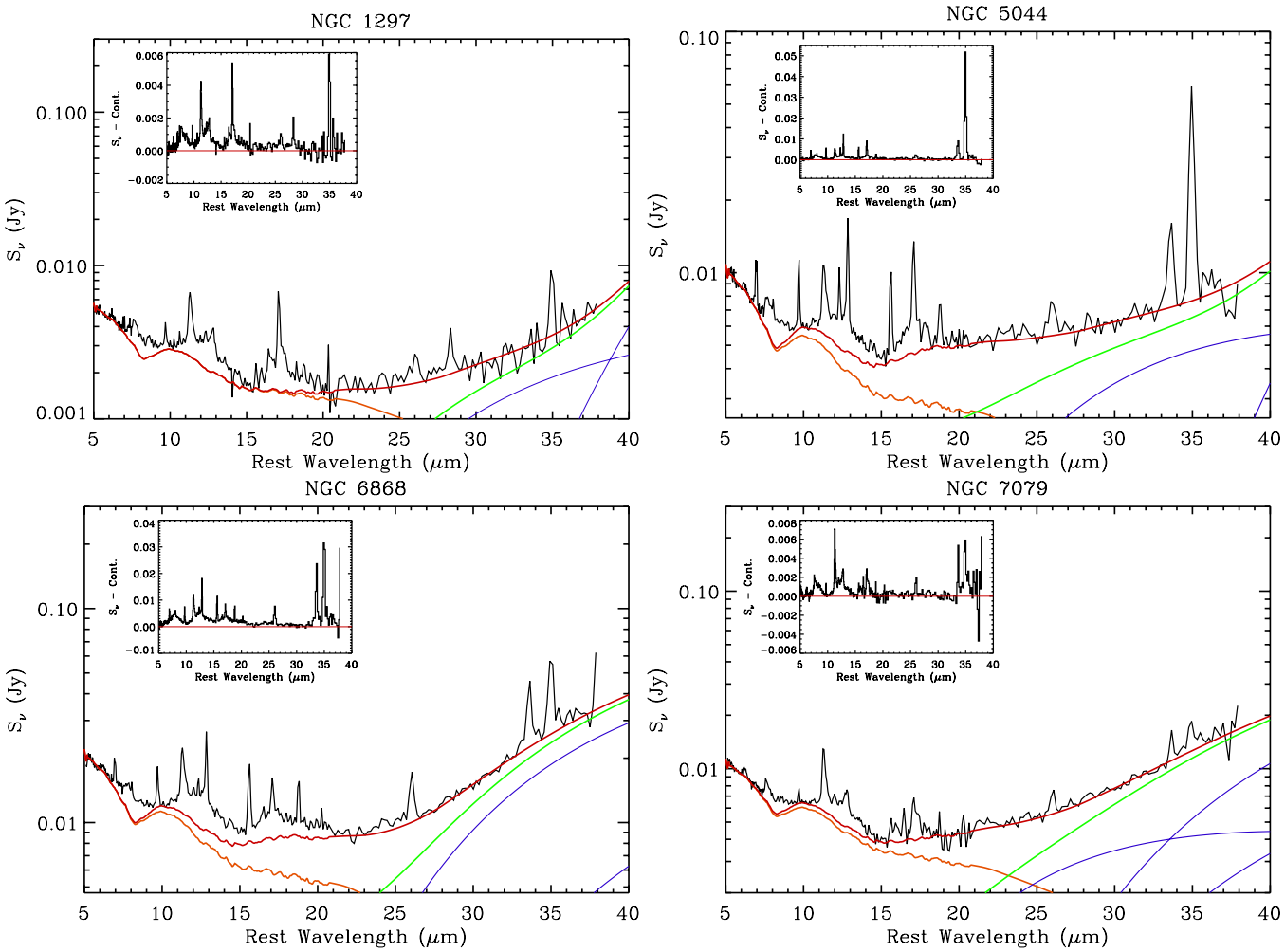

Figure 2. Detailed fit to the MIR continuum emission of our sample of ETGs. The orange line represents the template of the passive ETG normalized to the *H* band. Blue lines represent the different thermal dust components. The green line represents the sum of all dust components. The red line is the best-fit model to the total continuum emission, calculated as the sum of the normalized passive ETG plus the thermal dust components. In the insets, we plot the continuum-subtracted spectra. Note the broad feature around 8 μm that emerges when the continuum is subtracted.

(A color version of this figure is available in the online journal.)

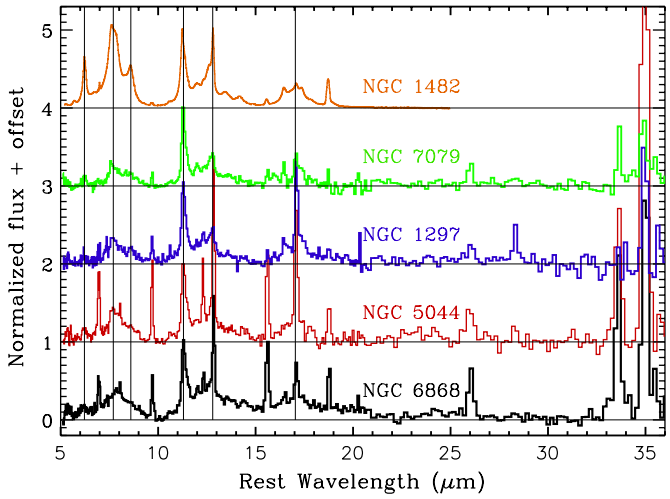

Figure 3. Continuum-subtracted spectra of our ETGs normalized to the peak intensity of the 11.3 μm feature. For comparison, we also show the IRS spectrum of NGC 1482, a SINGs H II galaxy from Smith et al. (2007). Vertical lines indicate the positions of the main PAH complexes at 6.2, 7.7, 8.6, 11.3, 12.8, and 17 μm.

(A color version of this figure is available in the online journal.)

3.2.1. The Individual Features

We use a spectral decomposition method similar to that outlined by Smith et al. (2007) to recover the PAH features and the emission lines. In this method, the spectrum is modeled by a combination of Gaussian profiles for the atomic and molecular emission lines, and Drude profiles for the PAH features (e.g., Li & Draine 2001). The broad PAH features are represented by up to four sub-features grouped as blended complexes, some of them adopted to best reproduce the band shape (e.g., Smith et al. 2007). In order to explore if the peculiarities of our PAH spectra could be due to not only differences in the relative intensities of the sub-features, but also differences in their characterizations, we leave as free parameters the central wavelengths, λ_0 and the fractional FWHM, γ, of the Drude profiles. The model is then fitted to the observed spectra by minimizing the global χ^2 using the Levenberg–Marquardt algorithm, and using the values λ_0 and γ reported by Draine & Li 2007 (hereafter DL07) as the initial guess for the parameters of the Drude profile.

The best fits to the spectra are shown as thick red lines in Figure 4, where the fitted PAH sub-features and emission lines are shown as thin green and thin orange lines, respectively. The results of the fits are summarized in Table 3. Columns 1 and 2

Table 3
Parameters and Integrated Fluxes of the Fitted PAH Features

DL07[a]		N1297[b]			N5044[b]			N6868[b]			N7079[b]		
λ_0^c	γ	λ_0^c	γ	F^d	λ_0^c	γ	F^d	λ_0^c	γ	F^d	λ_0^c	γ	F^d
5.27	0.034	5.25 ± 0.01	0.025 ± 0.006	5.76 ± 2.71	5.25 ± 0.01	0.025 ± 0.002	13.38 ± 5.37	5.25 ± 0.01	0.025 ± 0.005	40.51 ± 15.04	5.20 ± 0.01	0.034 ± 0.006	22.13 ± 10.17
5.70	0.035	5.70 ± 0.01	0.035 ± 0.015	1.37 ± 4.45	5.72 ± 0.01	0.035 ± 0.015	8.41 ± 5.17	5.70 ± 0.03	0.035 ± 0.015	16.69 ± 11.97	5.70 ± 0.01	0.035 ± 0.015	< 0.01
6.22	0.030	6.20 ± 0.04	0.050 ± 0.013	12.64 ± 7.24	6.22 ± 0.01	0.048 ± 0.007	27.89 ± 6.11	6.22 ± 0.01	0.048 ± 0.006	53.32 ± 10.64	6.22 ± 0.01	0.030 ± 0.008	19.41 ± 2.35
6.69	0.070	6.69 ± 0.15	0.070 ± 0.007	9.31 ± 6.87	6.69 ± 0.06	0.070 ± 0.010	15.69 ± 7.56	6.69 ± 0.06	0.070 ± 0.016	46.87 ± 19.06	6.69 ± 0.01	0.070 ± 0.007	7.65 ± 2.97
7.42[e]	0.126	7.42 ± 0.01	0.126 ± 0.005	1.74 ± 3.98	7.42 ± 0.01	0.126 ± 0.002	21.34 ± 5.08	7.42 ± 0.01	0.126 ± 0.002	142.61 ± 11.41	7.42 ± 0.01	0.126 ± 0.008	7.06 ± 0.80
7.60[e]	0.044	7.61 ± 0.01	0.050 ± 0.012	20.07 ± 0.97	7.62 ± 0.03	0.035 ± 0.008	26.59 ± 4.62	7.60 ± 0.01	0.044 ± 0.020	< 0.01	7.57 ± 0.01	0.040 ± 0.004	41.75 ± 5.94
7.85[e]	0.053	7.80 ± 0.01	0.078 ± 0.011	26.36 ± 1.35	7.90 ± 0.02	0.077 ± 0.005	55.77 ± 2.27	7.86 ± 0.01	0.077 ± 0.003	146.80 ± 3.01	7.86 ± 0.02	0.053 ± 0.004	35.21 ± 2.35
8.33	0.052	8.20 ± 0.01	0.050 ± 0.025	2.75 ± 2.37	8.29 ± 0.02	0.025 ± 0.010	3.72 ± 3.84	8.33 ± 0.01	0.035 ± 0.003	6.74 ± 1.10	8.33 ± 0.01	0.030 ± 0.006	16.07 ± 1.46
8.61	0.039	8.59 ± 0.02	0.040 ± 0.006	14.16 ± 0.79	8.60 ± 0.01	0.075 ± 0.002	27.46 ± 0.78	8.61 ± 0.01	0.080 ± 0.010	69.81 ± 2.76	8.61 ± 0.01	0.039 ± 0.005	17.54 ± 1.52
10.68	0.020	10.68 ± 0.08	0.020 ± 0.010	< 0.01	10.68 ± 0.02	0.020 ± 0.010	< 0.01	10.68 ± 0.02	0.020 ± 0.010	< 0.01	10.68 ± 0.05	0.020 ± 0.010	< 0.01
11.23[f]	0.012	11.23 ± 0.01	0.012 ± 0.002	9.13 ± 0.05	11.23 ± 0.01	0.012 ± 0.002	10.71 ± 0.36	11.23 ± 0.01	0.012 ± 0.002	20.65 ± 0.28	11.23 ± 0.01	0.012 ± 0.002	23.12 ± 0.11
11.33[f]	0.032	11.33 ± 0.01	0.032 ± 0.002	37.75 ± 0.22	11.33 ± 0.01	0.032 ± 0.003	46.76 ± 0.41	11.33 ± 0.01	0.032 ± 0.001	112.11 ± 1.06	11.33 ± 0.01	0.032 ± 0.002	40.85 ± 0.92
11.99	0.045	11.98 ± 0.03	0.025 ± 0.007	7.45 ± 1.68	11.99 ± 0.02	0.045 ± 0.003	15.32 ± 2.04	11.99 ± 0.01	0.034 ± 0.004	43.00 ± 4.19	11.97 ± 0.01	0.025 ± 0.005	13.82 ± 2.00
12.62[g]	0.042	12.62 ± 0.1	0.047 ± 0.004	19.53 ± 0.39	12.62 ± 0.01	0.047 ± 0.003	23.42 ± 1.64	12.62 ± 0.01	0.047 ± 0.002	63.49 ± 4.11	12.62 ± 0.01	0.047 ± 0.006	27.32 ± 1.32
12.69[g]	0.013	12.69 ± 0.01	0.013 ± 0.004	1.87 ± 1.12	12.69 ± 0.01	0.013 ± 0.002	2.84 ± 1.20	12.69 ± 0.01	0.013 ± 0.002	6.40 ± 2.01	12.69 ± 0.01	0.013 ± 0.002	4.06 ± 1.62
13.48	0.040	13.48 ± 0.04	0.070 ± 0.014	7.20 ± 0.85	13.43 ± 0.15	0.070 ± 0.009	15.72 ± 1.56	13.48 ± 0.04	0.070 ± 0.012	59.64 ± 2.20	13.50 ± 0.08	0.070 ± 0.011	17.08 ± 1.08
14.04	0.016	14.04 ± 0.05	0.016 ± 0.008	< 0.10	14.04 ± 0.17	0.016 ± 0.010	< 0.10	14.04 ± 0.09	0.016 ± 0.008	< 0.01	14.04 ± 0.10	0.016 ± 0.009	< 0.01
14.19	0.025	14.40 ± 0.04	0.025 ± 0.008	1.45 ± 0.69	14.40 ± 0.06	0.050 ± 0.015	10.05 ± 3.11	14.40 ± 0.04	0.050 ± 0.008	31.71 ± 3.47	14.40 ± 0.07	0.050 ± 0.009	3.31 ± 0.91
15.90	0.020	15.90 ± 0.04	0.015 ± 0.005	1.67 ± 0.08	16.05 ± 0.01	0.030 ± 0.004	3.65 ± 0.18	16.10 ± 0.07	0.030 ± 0.012	10.96 ± 0.49	15.90 ± 0.01	0.020 ± 0.004	5.51 ± 0.30
16.45[h]	0.014	16.39 ± 0.01	0.014 ± 0.003	3.51 ± 0.08	16.55 ± 0.01	0.014 ± 0.001	2.35 ± 0.65	16.45 ± 0.01	0.015 ± 0.003	8.76 ± 0.45	16.40 ± 0.01	0.015 ± 0.003	8.16 ± 0.35
17.04[h]	0.065	17.04 ± 0.01	0.065 ± 0.002	16.95 ± 0.15	17.04 ± 0.05	0.065 ± 0.001	18.46 ± 0.20	17.04 ± 0.01	0.065 ± 0.004	56.02 ± 0.87	17.04 ± 0.01	0.065 ± 0.003	2.57 ± 0.40
17.37[h]	0.012	17.37 ± 0.04	0.020 ± 0.005	2.79 ± 0.56	17.37 ± 0.02	0.012 ± 0.002	1.84 ± 0.51	17.37 ± 0.01	0.012 ± 0.009	2.78 ± 0.70	17.30 ± 0.02	0.025 ± 0.002	9.54 ± 0.72
17.87[h]	0.016	17.87 ± 0.18	0.016 ± 0.003	0.18 ± 0.07	17.70 ± 0.02	0.016 ± 0.003	2.34 ± 0.18	18.10 ± 0.02	0.016 ± 0.003	1.70 ± 0.17	17.86 ± 0.01	0.025 ± 0.003	1.93 ± 0.41
18.92	0.019	18.70 ± 0.25	0.010 ± 0.012	0.54 ± 0.04	18.70 ± 0.04	0.039 ± 0.005	2.10 ± 0.80	18.70 ± 0.01	0.039 ± 0.006	13.20 ± 0.64	18.70 ± 0.01	0.039 ± 0.004	3.31 ± 0.56
		19.15 ± 0.04	0.030 ± 0.010	2.05 ± 0.90	19.10 ± 0.01	0.030 ± 0.010	0.99 ± 0.22	19.10 ± 0.03	0.030 ± 0.007	6.52 ± 1.20	19.10 ± 0.01	0.030 ± 0.015	< 0.01

Notes.

[a] Central wavelength (λ_0) and fractional FWHM (γ) of the features from DL07.

[b] λ_0, γ, and integrated fluxes, F, of each feature given by our best fit to the MIR spectra.

[c] Units in μm.

[d] Units in 10^{-18} W m^{-2}.

[e] 7.7 μm complex.

[f] 11.3 μm complex.

[g] 12.7 μm complex.

[h] 17 μm complex.

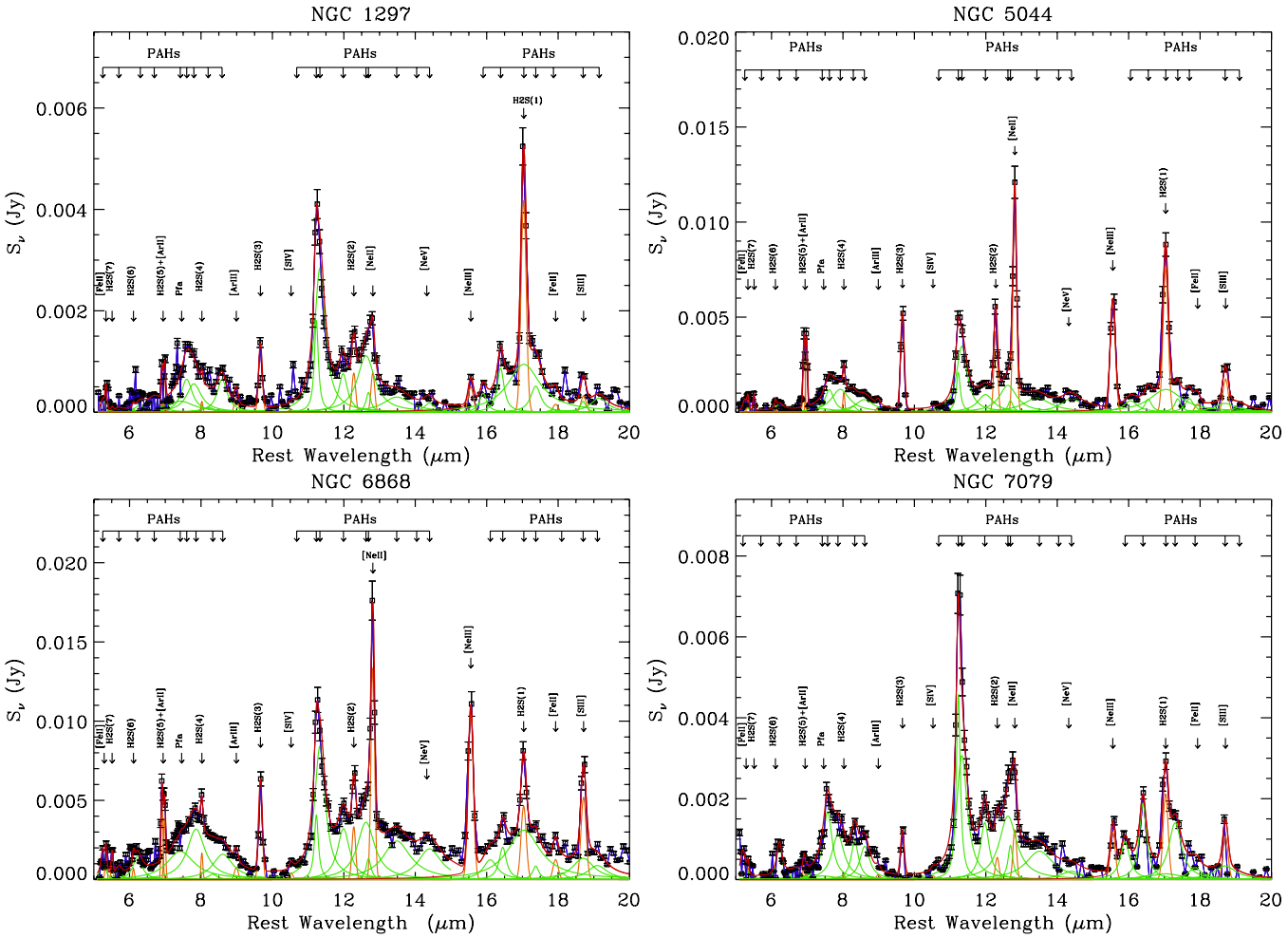

Figure 4. Detailed fit to the lines and the PAH emission for the continuum-subtracted spectra of NGC 1297 (upper left), NGC 5044 (upper right), NGC 6868 (lower left), and NGC 7079 (lower right) in the spectral region between 5 and 20 μm. The open squares and the blue solid line indicate the observed MIR continuum-subtracted spectra. The solid red line indicates the total fit to the data, calculated as the sum of the PAH features (solid thin green lines) and the emission lines (solid thin orange lines). Arrows indicate the positions of the fitted PAH features, nebular emission lines, and H_2 rotational lines.

(A color version of this figure is available in the online journal.)

list the central wavelengths, λ_0 and the fractional FWHM, γ, reported by DL07.

In the remaining columns we report, for each galaxy, the fitted λ_0, γ, and the corresponding integrated fluxes. Different sub-features of the 7.7 μm, 11.3 μm, 12.7 μm, and 17 μm PAH complexes, are indicated with the letters a, b, c, and d, respectively. The errors in the derived fluxes and Drude profile parameters have been estimated repeating the above procedure with simulated spectra obtained by randomly varying the fluxes within the observational error. The process was repeated 100 times and the errors were calculated as the standard deviation of the distribution of the fitted values in the simulations.

From Table 3 we note that even though most of the λ_0 and γ of the fitted features are in good agreement with those reported by DL07, the fits for NGC 6868, NGC 5044, and to a lesser extent NGC 1297, required some Drude profiles with significantly different lambda peaks and/or fractional FWHM. For some features the differences may be due to low signal to noise (i.e., 5.27 μm) but this is not the case for the 7–9 μm complex, which is well detected in all cases.

The most remarkable differences with respect to DL07 are as follows.

1. The weakness or even lack of the 7.6 μm feature in NGC 5044 and NGC 6868. The 7.6 μm feature is the main component of the 7.7 μm complex in normal and active galaxies (e.g., Peeters et al. 2004; Smith et al. 2007; Tielens 2008).
2. The brightest component is the 7.85 μm sub-feature. It is also about twice as wide ($\gamma \sim 0.077$) as that in DL07. Moreover, in the case of NGC 5044, it peaks at $\lambda_0 = 7.90\,\mu$m.
3. The fits to the broad 6–9 μm feature in the NGC 5044 and NGC 6868 spectra also require two times wider ($\gamma \sim 0.75$–0.8) Drude profiles for the 8.6 μm feature.
4. The 17 μm PAH complex is also wider than in normal galaxies and requires an "extra" feature at about 19.1 μm.

The fitting requirements of wider Drude profiles for the well-established features at 7.7 μm and 8.6 μm are actually due to an emission excess in the 6–9 μm spectral range with respect to what is recovered by using only the *standard* PAH Drude profiles (i.e., DL07's features). Thus, the broad 6–9 μm feature in NGC 5044 and NGC 6868 could also be well reproduced by adding some *extra* Drude profile sub-features to the *standard* PAH feature set.

In order to test if this *excess* emission could be due to the use of a different decomposition method to that used by Smith et al. (2007), we applied our procedure to NGC 4435 (Panuzzo et al. 2007) and to NGC 1482 (Smith et al. 2007) from the Smith et al.

Table 4
PAH Inter-band Ratios and PAH-to-Continuum Ratios

Ratios	N1297	N5044	N6868	N7079	SINGs Median Value[b]
6.2/7.7[a]	0.20 ± 0.11	0.15 ± 0.06	0.18 ± 0.04	0.23 ± 0.03	0.28 [0.21–0.34]
6.2/11.3[a]	0.27 ± 0.10	0.47 ± 0.11	0.40 ± 0.09	0.30 ± 0.04	1.10 [0.77–1.43]
6.2/17[a]	0.54 ± 0.31	0.51 ± 0.21	0.77 ± 0.15	0.87 ± 0.11	1.90 [1.33–2.47]
7.7[a]/11.3[a]	1.36 ± 0.09	1.80 ± 0.13	2.18 ± 0.09	1.26 ± 0.10	3.60 [2.52–4.68]
7.7[a]/8.6	3.40 ± 0.36	3.77 ± 0.28	4.14 ± 0.23	4.79 ± 0.55	5.70 [3.99–7.41]
7.7[a]/17[a]	2.72 ± 0.20	3.34 ± 0.26	4.18 ± 0.18	3.78 ± 0.33	6.90 [4.83–8.97]
8.6/11.3[a]	0.31 ± 0.04	0.47 ± 0.03	0.53 ± 0.02	0.27 ± 0.02	0.68 [0.48–0.88]
11.3[a]/12.7[a]	2.19 ± 0.12	2.18 ± 0.17	1.90 ± 0.13	2.03 ± 0.14	1.80 [1.26–2.39]
17[a]/11.3[a]	0.50 ± 0.01	0.44 ± 0.02	0.52 ± 0.01	0.35 ± 0.02	0.53 [0.37–0.69]
$L_{\rm PAH}(6.2)/\nu L_\nu(24)$	0.058 ± 0.034	0.039 ± 0.009	0.044 ± 0.010	0.031 ± 0.005	0.10 [0.05–0.20]
$L_{\rm PAH}(7.7)/\nu L_\nu(24)$	0.220 ± 0.029	0.148 ± 0.010	0.240 ± 0.025	0.132 ± 0.017	0.40 [0.25–1.00]
$L_{\rm PAH}(11.3)/\nu L_\nu(24)$	0.215 ± 0.022	0.082 ± 0.008	0.110 ± 0.011	0.101 ± 0.010	0.10 [0.04–0.20]
$L_{\rm PAH}(17)/\nu L_\nu(24)$	0.107 ± 0.011	0.038 ± 0.004	0.057 ± 0.006	0.035 ± 0.004	0.06 [0.03–0.10]

Notes.
[a] Blended PAH complex, see Table 3.
[b] Median value and 1σ variation in the corresponding ratio derived by Smith et al. (2007) for the SINGs galaxy sample.

sample. In neither case did we find significant differences with respect to the values reported by DL07. By using the NGC 1482 spectrum we also test the dependence of our results on the different methods of subtraction of the underlying continuum. Following the recipe described in Section 3, we find that the contribution from the old stellar population to the 5.6 μm flux is $< 28\%$, and that the differences between the continuum-subtracted spectrum obtained with our method and with PAHFIT (Smith et al. 2007) are negligible. Thus, we are confident that our results are not an artifact of the adopted method for the subtraction of the underlying continuum. Note, however, that for a correct subtraction of the stellar component, the use of a proper stellar template is mandatory for ETGs at odds with H II galaxies where the contribution of the old stellar population to the MIR spectral range is small.

3.2.2. PAH Inter-band Ratios

The strengths of the individual PAH bands are affected by a variety of mechanisms that include the distribution of PAH sizes and charges, PAH de-hydrogenization, and the strength and hardness of the radiation field exciting the PAHs (e.g., Tielens 2008; Galliano et al. 2008). Possible destruction mechanisms of PAHs are also varied, including photodissociation, sputtering, and dissociation in shocks (e.g., Leger et al. 1989; Micelotta et al. 2010a, 2010b). Variations of the PAH inter-band ratios can be explained by the combined effects of those mechanisms, and hence to variations in the physical conditions of the environment (e.g., Allamandola et al. 1989; Schutte et al. 1993; Draine & Li 2007; Galliano et al. 2008; Tielens 2008).

Table 4 lists the ratios of the strongest PAH bands. In the last column of the table, we report the median values and their 1σ variation for the 59 objects of the SINGs galaxy sample (Smith et al. 2007). The most striking characteristic of the spectra is the unusually low 7.7/11.3 μm PAH inter-band ratio with respect to what is observed in star-forming galaxies. This unusual ratio was already reported by Kaneda et al. (2005) and Bressan et al. (2006b) in a small set of ETGs and later confirmed by Kaneda et al. (2008) for a larger sample of ETGs and by Smith et al. (2007) for a subset of about 10 objects in the SINGs galaxy sample. A more careful inspection of the spectra indicates that the 7.7/11.3 μm PAH inter-band ratio is not alone in presenting these unusual values but there is a systematic deficit in the shorter wavelength bands (i.e., 6.2, 7.7, and 8.6 μm) with respect to those peaking at longer wavelengths (i.e., 11.3, 12.7, and 17 μm). This effect is more extreme at shorter wavelengths, with the 6.2 μm band having the strongest deficit. The average 6.2/11.3 ratio for our four galaxies is 0.36 ± 0.20 which is significantly different from 1.10 ± 0.33 of the SINGs galaxies. The same for 6.2/17; ours is 0.67 ± 0.30 while SINGs' is 1.9 ± 0.57. Differences in the 7.7/11.3 and 7.7/17 μm ratios are less extreme. Our average 7.7/11.3 and 7.7/17 μm ratios are 1.65 ± 0.54 and 3.51 ± 0.80, while the mean values for the SINGs sample are 3.60 ± 1.08 and 6.90 ± 2.07, respectively. In the case of the 8.6 μm band, only NGC 1297 and NGC 7079 present 8.6/11.3 μm and 8.6/11.3 μm ratios which are significatively lower than the values of the SINGs sample. Whereas, 17/11.3 μm and the 12.7/11.3 μm ratios are, in all the cases, within the values found for the SINGs galaxy sample. We check whether these differences could be due to some general PAH emission defect with respect to dust emission. In the last rows of Table 4, we report the ratio between PAH complexes and the $\rm MIPS_{24\,\mu m}$ luminosity. The last column also provides the median values of the SINGs sample. We see again that the deficit is selective, and it occurs only in the shorter wavelength bands, while at 11.3 μm and 17 μm, the ratios fall within those of the SINGs sample.

Laboratory studies and theoretical calculations show that the 6–9 μm bands are intrinsically weak in neutral PAHs and become stronger when the PAHs are ionized (Allamandola et al. 1999; Bauschlicher 2002; Kim & Saykally 2002). Therefore, the 6–9 μm bands will be much more intense for an ionized PAH than for a neutral PAH, while the contrary will be true for the 3.3 and 11.3 μm bands. Consequently, the ratios between the 6–9 μm bands and the 11.3 μm band depend on the charge of the PAHs, which is directly related to the physical conditions (intensity of the ionizing radiation field, electron density, etc.) of the PAH emitting region. On the other hand, larger PAHs attain lower temperatures than their smaller counterparts upon the absorption of the same photon. That implies that smaller PAHs will contribute mainly at short wavelengths, while larger PAHs account mainly for the emission at long wavelengths (e.g., Schutte et al. 1990, 1993; Draine & Li 2007; Bauschlicher et al. 2008, 2009; Boersma et al. 2010). Boersma et al. (2010) found that while the 6–9 μm and 11.3 μm bands are very sensitive to the ionization state of the PAH molecule, the 17 μm complex is not, and that the emission of this complex is probably due to the C–C–C vibrational modes of a limited number of large

PAHs. Consistently, the ratios of the 17/6–9 μm features would be a sensitive probe of the size of interstellar PAHs so that size distributions biased to large PAHs would result in higher values of the 17/6.2 μm and 17/7.7 μm ratios compared to the values in normal galaxies. On the other hand, charge distributions biased to neutral PAHs will result in lower 7.7/11.3 μm and 6.2/11.3 μm ratios compared to those in normal galaxies.

Therefore, the low values of the 6.2/17 μm and the 7.7/17 μm ratios in our ETGs imply a size distribution deficient in small PAHs, and responsible for the "normal" PAH emission at 17 μm. This suggestion is reinforced by the small values of the 6.2/7.7 μm ratio which is particularly sensitive to the lower cutoff of the PAH size distribution (e.g., Draine & Li 2007; Galliano et al. 2008). However, theoretical computations of large ionized PAH spectra indicate an enhanced emission of the 6–9 μm bands with respect to the 11.3 μm band, even if the temperature cascade effects are taken into account in their computations (see Figure 17 of Boersma et al. 2010). Therefore, a mixture of large PAHs with a *normal* charge distribution could not reproduce the low values of the 7.7/11.3 μm ratios observed in our objects, which would require of a mixture plentiful of neutral PAHs. In summary, the low values of the 6–9 μm bands versus the 11.3 μm and the 17 μm bands observed in our objects are compatible with the emission from a mixture that is rich in large and neutral PAHs.

4. CHARACTERIZATION OF THE PAH EMISSION

Instead of using combinations of single Drude profiles, we will now analyze the continuum-subtracted spectra by means of *emission templates* of different dust components. We will follow the method devised by Rapacioli et al. (2005), Berné et al. (2007), Joblin et al. (2008), Joblin et al. (2009), and Berné et al. (2009) which provides general information on the sizes and ionization states of PAHs, and the presence of other dust components. In this way, we will gain insight into the nature of these spectral features and, ultimately, about the stellar populations and physical processes involved. Before using the emission templates, we removed the emission lines from the continuum-subtracted spectra by using the values of the lines derived in the fits performed in Section 3.2.

4.1. The Templates

There are several studies in the literature about emission templates of PAH families and other dust features (e.g., Cesarsky et al. 2000; Rapacioli et al. 2005, 2006; Berné et al. 2007; Joblin et al. 2008, 2009; Berné et al. 2009). For the following analysis we will use the PAH–dust feature templates from Joblin et al. (2008) which are shown in Figure 5. The parameters of the templates (i.e., λ_0 and FWHM of the Lorentzian and Gaussian profiles) were taken from their Table A.1. Three of them were obtained from the mathematical decomposition of three reflection nebulae observed with *ISO* and *Spitzer* by using the Principal Component Analysis technique (Rapacioli et al. 2005; Berné et al. 2007). The first template, called PAH$^+$, characterized by strong C–C modes (6–9 μm) relative to C–H modes (10–14 μm) and peaking at 7.6 μm, is attributed to PAH cations (Rapacioli et al. 2005). The second template called PAH^0, characterized by strong C–H modes relative to C–C modes and showing an evident peak at 11.3 μm, is attributed by the authors to a PAH mixture rich in neutral PAHs (Rapacioli et al. 2005). The third one called VSG consists of weaker and broader features and is likely due to PAH clusters (Cesarsky et al. 2000; Rapacioli et al. 2005; Rapacioli et al. 2006). The same authors suggest that PAH clusters could break into free PAHs under the effects of a UV radiation field.

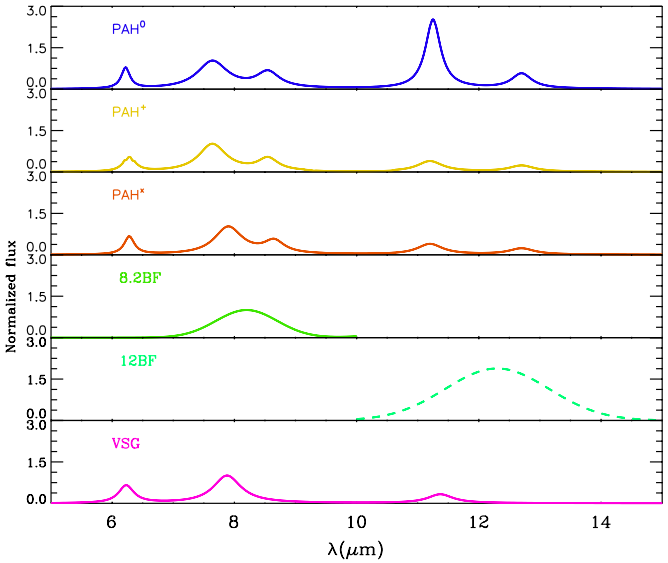

Figure 5. Templates from Joblin et al. (2008). Fluxes are normalized to the peak of the 7.7 μm component.

(A color version of this figure is available in the online journal.)

The other three observational components were later introduced by Joblin et al. (2008). They were required by those authors to fit the spectra of Galactic and magellanic cloud planetary nebulae (PNe) observed with *Spitzer* and *ISO*, which could not be fitted only with the templates derived by Rapacioli et al. (2005). Two of them are broad emission features (BF) at 8.2 μm and 12 μm already seen in some post-AGB stars (Kwok & Hrivnak 1989; Hrivnak et al. 2000; Hony et al. 2001; Peeters et al. 2002; van Diedenhoven et al. 2004; Szczerba et al. 2005; Kraemer et al. 2006). Peeters et al. (2002) classified as C-class objects those in which the broad 8.2 μm feature is observed. The 8.2 BF and the 12 BF templates were built by Joblin et al. by fitting those observed bands in the post-AGB star IRAS 13416-6243 MIR spectrum, which is classified as a C-class object prototype by Peeters et al. (2002). It is worth recalling that the contributions of the broad features (BFs; i.e., 8.2 BF and 12 BF) are important only for the objects that are thought to be in *transition* from the AGB to the PN phase (e.g., Peeters et al. 2002; van Diedenhoven et al. 2004; Sloan et al. 2007; Tielens 2008; Joblin et al. 2009; Berné et al. 2009). The second one is a "new" PAH type template spectrum, named *PAH*$^{\rm x}$, with the 7.8 μm band shifted to 7.9 μm and the 8.55 μm shifted to 8.65 μm. This template was introduced "ad hoc" by Joblin et al. (2008), who tentatively associated it with large ($N_C \geqslant 100$) PAHs, likely anions, although the large cations option could not be excluded (Bauschlicher et al. 2008, 2009).

With the empirical templates, we obtained best fits like that shown in Figure 6 for NGC 6868. Though the best fit represents fairly well the general shape of the PAH spectrum, we find that it underestimates significantly the flux of the 11.3 μm feature. In Figure 7, we show the best fit for NGC 1482. In this case, the MIR spectrum is well reproduced with the set of templates, indicating that, at odd of our ETGs, the *usual* PAH spectrum can be depicted by a variable combination of these dust components, mainly by PAH$^+$, PAH^0, and VSG. Since the 7.7/11.3 μm ratio is one of the main peculiarities of the observed spectra and the

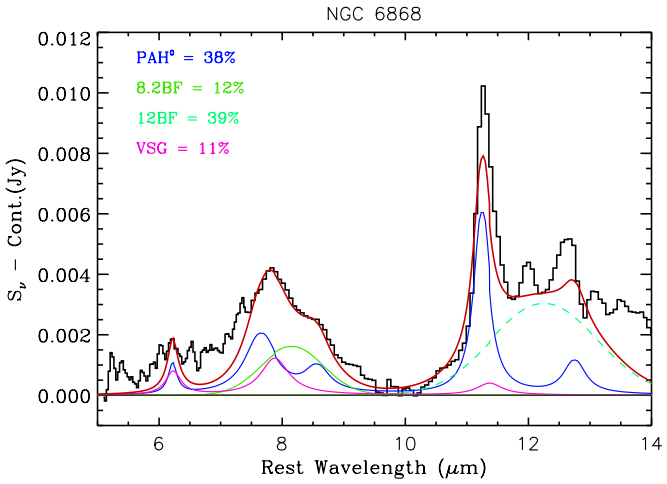

Figure 6. Analysis of the PAH spectrum of NGC 6868 after emission line subtraction (solid black line) with the template spectra displayed in Figure 5. The best fit is shown as a solid red line, while the contribution of each PAH component is shown with the same color code as in Figure 5. In the legend, we display the percentage contribution of the different PAH components to the integrated flux in the range between 5.5 and 14 μm.

(A color version of this figure is available in the online journal.)

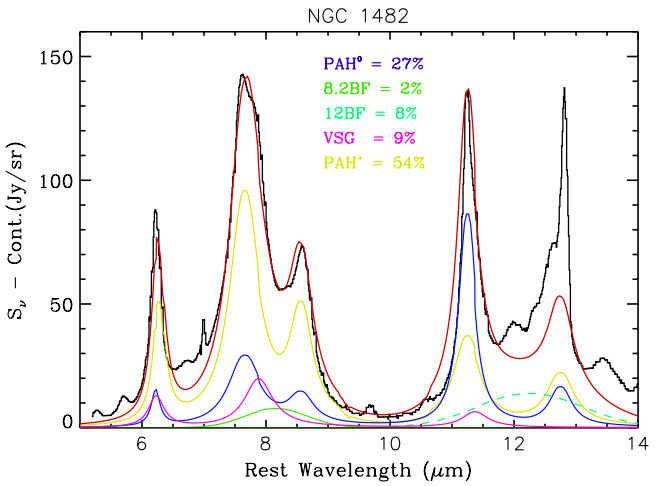

Figure 7. Fit to the continuum-subtracted spectrum of the H II galaxy NGC 1482 (Smith et al. 2007) by using the set of nine dust feature template spectra. The meaning of the lines is as in Figure 8. Note that the main contributor to the integrated flux is the PAH cations, as is expected in an object with a burst of star formation (Allamandola et al. 1999). The BF contributions are very small.

(A color version of this figure is available in the online journal.)

problem affects all our fits, it may indicate that the adopted templates, in particular the PAH^0 component, are not fully adequate.

Tielens (2008) points out that the PAH^0 template shows more emission in the 6–9 μm region than that expected from theoretical calculations and laboratory studies of neutral PAHs. The same author suggests two different possibilities to explain this discrepancy: (1) the PAH^0 template could represent the particular mixture of PAHs, which could be dominated by neutral PAHs but with some, likely small, contribution from ionized PAHs, and/or (2) it could also reflect the effect of the size on the intrinsic spectrum of neutral PAHs. The latter point might indicate that the emitting PAH mixture in our ETGs has a size distribution more biased toward large and neutral PAHs, than that one characterizing the PAH^0 component.

To bypass these difficulties we also include in our set of templates the theoretical spectra of a mixture of 10 large, compact, and highly symmetric neutral, cationic, and anionic, PAHs, L-PAH^0, L-PAH$^+$, L-PAH$^-$, respectively, derived by Bauschlicher et al. (2008, see their Figure 6). In order to compare those theoretical *absorption* PAH spectra with observed PAH *emission* spectra, band shapes, widths, and shifts inherent to the emission processes must be taken into account (Bauschlicher et al. 2008, 2009). Therefore, we followed the recommendations of Bauschlicher et al. (2008, 2009) concerning the fitting of astronomical PAH spectra, and we redshifted the computed spectra by a value of 15 cm^{-1}, and used a bandwidth of 30 cm^{-1} for the bands shortward of 9 μm, and 10 cm^{-1} for the bands longward of 10 μm.

The results of the new fits are shown in Figure 8, where the 11.3 μm feature is now well fitted in all cases. In Table 5, we report the corresponding fractional contributions of the single PAH templates to the best fits. The PAH spectra of our ETGs are reproduced well with only a few dust feature components: the PAH^0 and L-PAH^0, the BF components (i.e., 8.2 BF + 12 BF), and the VSGs. Particulary striking is the evident deficit of the PAH$^+$ emission component, which is the main contributor in H II regions and normal galaxies, see Figure 7 (e.g., DL07; Tielens 2008 and references therein). Even if the PAH^0 and the

Table 5
Relative Contribution in Percentage of the Different Dust Feature Components to the Integrated Fluxes of the ETGs

Galaxy	PAH^0	PAH$^+$	8.2 BF[a]	12 BF[a]	BF[a] (8.2 + 12)	VSG	L PAH^0
NGC 1297	61	...	9 (11)	26 (30)	35 (41)	...	4
NGC 5044	43	5	10 (11)	26 (34)	36 (45)	9	7
NGC 6868	35	...	12 (13)	36 (38)	48 (51)	7	10
NGC 7079	58	...	8 (10)	24 (29)	32 (39)	...	10

Note. [a] Values in parenthesis correspond to the relative contribution in percentage of the BF components to the integrated fluxes of the ETGs in the case of the Virgo stellar continuum template subtraction, see the text for details.

L-PAH^0 components dominate the total PAH emission, suggesting that the main PAH contributors could be likely the neutral PAHs, we cannot completely discard the presence of ionized PAHs in the PAH mixture. That is, because, on the one hand, the PAH^0 component can contain some contribution from ionized PAHs (Tielens 2008), and on the other, we are using an L-PAH theoretical spectra which was computed without including the temperature cascade effects. Boersma et al. (2010) show that the inclusion of the PAH temperature cascade in the calculations affects the relative band intensities. In that case, the intensities of the C–H and C–C–C bands increase significatively with respect to the C–C bands (see Figure 18 in Boersma et al. 2010), and therefore the fractional contribution of large ionized PAHs to the PAH mixture in our galaxies could be greater than expected from the previous analysis. However, even when some contribution from the ionized PAHs could be expected, the main result of our analysis still remains, i.e., the PAH spectra of our ETGs are dominated by emission from large and neutral PAH molecules. Moreover, Kaneda et al. (2007a) reported unusual 7.7/11.3 μm inter-band ratio in addition to no-significant PAH emission at 3.3 μm in the near to mid-IR spectrum of the ETG NGC 1316. As the 3.3 μm emission is usually attributed to emission from small, neutral PAHs, Kaneda et al. conclude that the overall near to mid-IR PAH spectrum can be explained by emission from large and neutral PAH molecules.

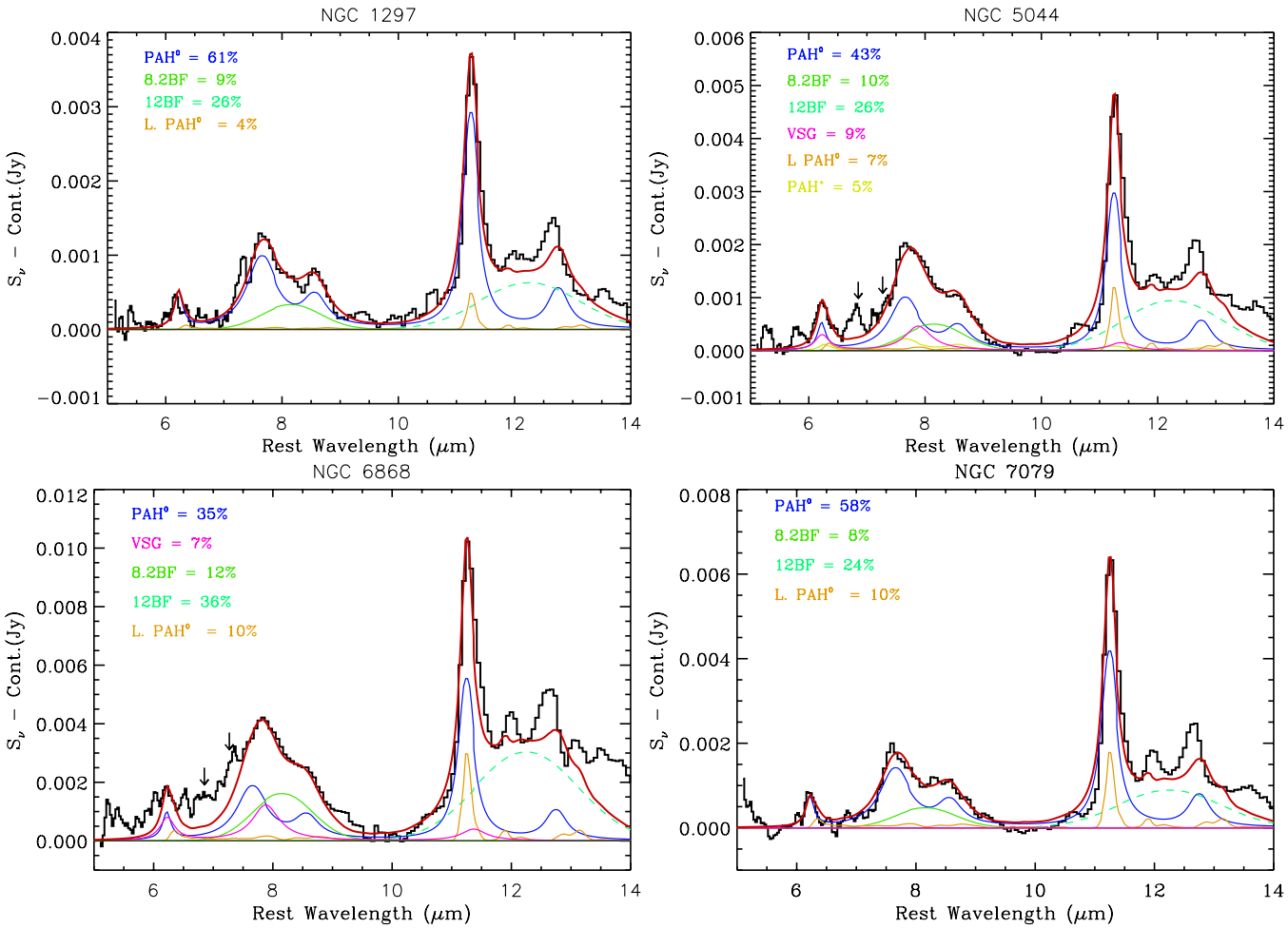

Figure 8. Best fits (solid red line) to the PAH spectra of our ETGs (solid black line). The different templates are shown in color: PAH^0(solid blue line), 8.2 BF component (solid green line), 12 BF component (dashed cyan line), VSG (solid magenta line), and large neutral PAHs (solid orange line). In the legend of each panel, we report the percentage of the relative contribution of the different dust feature components to the integrated flux in the range 5.5–14 μm. Arrows in the spectra of NGC 5044 and NGC 6868 indicate the possible detections of the 6.85 μm and 7.25 μm features usually ascribed to aliphatic material (e.g., Chiar et al. 2000; Sloan et al. 2007).

(A color version of this figure is available in the online journal.)

4.2. The Broad Feature Components

The other important contribution that we find in our galaxies is the BF components (i.e., 8.2 BF + 12 BF) which is, in all cases, higher than 30%, and even higher than the neutral component in NGC 6868.

Those components are needed to fill the broad 7–9 μm and 11–12 μm features. In particular, the 8.2 BF component would fill out the emission *excess* in the 6–9 μm spectral region mentioned in Section 3.2.1. At first glance, it could seem that by subtracting the passive ETG template, we have artificially enhanced the broad 7–9 μm feature, and that, as a consequence, we need to explain its strength by invoking a *broad* emission feature, identified as the 8.2 BF component. First of all, our objects are ETGs and a large fraction of their stellar populations must be old and quite metal rich (see Table A.1 in the Appendix); thus, the presence of the old stellar template is well justified. In addition we adopted a template of the passive galaxies in the field, which have a less pronounced 8 μm dip than Virgo cluster elliptical galaxies (see Figure 1). We also checked how the selection of a particular template of an old stellar population influenced our results. We repeat the analysis by using a template based on passive ETG members of the Virgo cluster. The results of the analysis are indicated in parenthesis in Table 5. Finally, the BF component has an even larger broad contribution around 12 μm (12 BF component) and, although in this region the fit is not perfect, the presence of this component strongly reduces the discrepancy with the observed spectra. As a further check we analyzed with the same technique the NGC 1482 spectrum (see Figure 7) which, at odds with our ETGs, is well reproduced by a mixture dominated by PAH cations, as expected in an H II galaxy (e.g., DL07), while the BF component is very small. In particular, the 8.2 BF component is negligible. We then suggest that the presence of the BF component is not an artifact of the analysis.

So far, the BF features have been detected only in a few objects, likely C stars in transition from the AGB phase to the PN phase (e.g., Buss et al. 1993; Peeters et al. 2002; Sloan et al. 2007; Joblin et al. 2008). However, Sloan et al. (2005) report broad and prominent features peaking at ∼8.3 μm in the MIR spectra of some protoplanetary disks around T-Tauri stars, and suggest that those BFs are the same as those found in the MIR spectrum of evolved stars (C-class objects from Peeters et al. 2002). Bouwman et al. (2008) and Berné et al. (2009) instead suggest that the BFs in T-Tauri stars present different peaks and

Table 6
Observed Lines Ratios, UV Magnitudes, and Derived Quantities

	N1297	N5044	N6868	N7079
[S III]18.7/[S III]33.5	0.37 ± 0.10	0.35 ± 0.15	0.36 ± 0.10	0.38 ± 0.12
$H_2S(3)/H_2S(1)$	0.66 ± 0.09	1.49 ± 0.30	2.85 ± 0.21	1.32 ± 0.15
[Ne III]15.5/[Ne II]12.8	0.61 ± 0.02	0.52 ± 0.01	0.74 ± 0.01	0.91 ± 0.02
[S III]33.5/[Si II]34.8	0.22 ± 0.02	0.21 ± 0.01	0.80 ± 0.04	0.98 ± 0.07
$m_{1516\,\text{Å}}$	...	20.05 ± 0.12	19.97 ± 0.10	21.10 ± 0.14
n_e (cm^{-3})	0.1–400	0.1–400	0.01–400	0.1–400
G_{FUV} (Habing units)[a]	...	0.51	0.54	0.20
$G_{FUV}T_{gas}^{1/2}/n_e$ ($K^{1/2}cm^3$)	...	<100	<110	<50

Note. [a] The flux of the Habing fields, $G_{FUV} = 1$, equals 2.3×10^{-3} erg cm^{-3} s^{-1} at $\lambda \sim 1530$ Å (Mathis et al. 1983).

widths than those of the C-class objects. Berné et al. (2009) argue that, since the chemical conditions in protoplanetary disk and evolved stars are different, there is no reason to suppose that the species causing the BFs in protoplanetary disks are the same as those producing the BFs in evolved stars. Since the spectra of our galaxies are well fitted with the parameters of 8.2 BF and 12 BF templates, built from the spectrum of the C-class object prototype, we assume that the BF emission in our galaxies is caused by the same material present in the C-class objects.

The actual carriers of the BF emission are still unknown. These features are commonly attributed to carriers rich in aliphatic material (e.g., Goto et al. 2003; Sloan et al. 2007; Joblin et al. 2008). However, Cami and coworkers find that the MIR spectrum of the C-class prototype object, IRAS 13416-6243 can be well reproduced with a mixture of small PAH spectra from the NASA Ames PAH spectral database (J. Cami et al. 2010, in preparation; see Figure 11 in Tielens 2008). Regardless of the actual carrier, which is out of the scope of this work, the key point here is that this material seems to be just created in the circumstellar envelopes of C-rich stars and later processed and/or destroyed by the stronger ISM UV fields. This will be later discussed deeper in Section 6.3. In any case, our tentative detections of the aliphatic bands at 6.85 μm and at 7.25 μm (e.g., Chiar et al. 2000; Sloan et al. 2007) in the spectra of NGC 5044 and NGC 6868 (see Figure 7) favor the aliphatic material interpretation. In that scenario, the BF spectra should arise from mixtures of aromatic and aliphatic carbon that have not yet been processed by intense ultraviolet radiation, allowing the more fragile aliphatic bonds to survive (e.g., Goto et al. 2003; Sloan et al. 2007; Joblin et al. 2008; Tielens 2008). A possible evolutionary scenario for such features is also proposed: in cool and less evolved C stars (in the post-AGB phase), the emission is dominated by this material. In a hotter ISM environment, the feature disappears because the aliphatic material has been processed into aromatic material (e.g., Goto et al. 2003; Sloan et al. 2007; Joblin et al. 2008). In this way, the presence of the BF features in our spectra would indicate the presence of pristine material.

5. THE INTERSTELLAR RADIATION FIELD

The analysis performed above suggests that the unusual PAH inter-band ratios seen in ETGs are due to changes in the size and charge distributions of the PAH mixture, which would be composed mainly of large and neutral PAH molecules. In this section, we consider the physical conditions in the ISM and whether or not they can account for such a PAH mixture.

5.1. The PAH Charge Distribution

The charge state of PAHs is mainly determined by the ionization parameter, $G_{FUV}T_{gas}^{1/2}/n_e$ (see Bakes et al. 2001; Tielens 2005) where G_{FUV} is the integrated far ultraviolet (900–2000 Å) radiation field in Habing radiation field units, T_{gas} is the gas temperature in Kelvins, and n_e is the electron density in cm^{-3}. In order to estimate the values of the ionization parameter for our objects, we use the values of the [S III]18.7/[S III]33.5, the $H_2S(3)/H_2S(1)$ line ratios, and the *GALEX* far-ultraviolet ($\lambda = 1516$ Å, $\Delta\lambda = 268$ Å) magnitudes within the central 5 arcsec from Marino et al. (2010), all reported in the Table 6, to quantify the electronic density, the gas temperature, and the integrated far ultraviolet radiations field, respectively. The derived [S III]18.7/[S III]33.5 line ratios are compatible with mean interstellar electronic densities, n_e between 0.1 and 300 cm^{-3} (Dale et al. 2006). Turner et al. (1977) showed that $H_2S(3)/H_2S(1)$ line ratios ranging from 0.6 to 3 correspond to gas temperatures of 150–400 K. Finally, by assuming the distances reported in Table 7, the FUV magnitudes correspond to average intensities of the interstellar FUV radiation field, in Habing units, of $G_{FUV} = 0.51, 0.54, 0.20$ for NGC 5044, NGC 6868, and NGC 7079, respectively, which are about half the Galactic value. In the last row of Table 6, we also display the corresponding ionization parameters, $G_{FUV}T_{gas}^{1/2}/n_e$, calculated for those three galaxies. The derived values are in agreement with the expected values from the quantification of the 6.2/11.3 μm ratio and the 7.7/11.3 μm ratio as a function of the ionization parameter given by Flagey et al. (2006) and/or by Galliano et al. (2008).

We roughly estimate the fraction of neutral PAHs by following Tielens (2005). In this case, the values of the averaged ionization parameter of our objects (i.e., $G_{FUV}T_{gas}^{1/2}/n_e \sim 100$) are compatible with a PAH mixture where even the 99% of the PAHs as large as ~1000 C-atoms are neutral. Lower values of the ionization parameter would indicate that even larger PAHs would be neutral.

5.2. The PAH Size Distribution

Panuzzo et al. (2010) show that a diagram of the [Ne III]15.5/[Ne II]12.8 versus the [S III]33.5/[Si II]34.8 ratio allows the different excitation mechanisms in galaxies, i.e., starburst photoionization, AGN photoionization, and shock heating, to be distinguished. Using this diagram, the values of those line ratios for our ETGs, listed also in Table 6, are accounted for by the shock+precursor models from Allen et al. (2008), with shock velocities < 150 km s^{-1}, pre-shock gas densities between 0.01–500 cm^{-3} and solar abundances, indicating that relatively

fast shocks in a low density medium is the primary powering mechanism in those LINERs. Micelotta et al. (2010b) analyze PAH processing in shocks by collisions with ions and/or electrons, and show that PAHs with $N_C < 200$ are completely destroyed by shocks with velocities $\sim$ 100–150 km s^{-1}, and only PAHs with sizes $N_C > 200$ could partially survive for a time of $\lesssim$ (1–4) $\times$ 10^8 yr. Fast shocks could be originated from jet-driven flows or accretion onto a massive black-hole, (e.g., Nagar et al. 2005; Dopita et al. 1997), or from turbulent motion of gas clouds, either injected by stellar mass loss (Bregman & Parriott 2009) or accreted, within the potential well of the galaxy. However, independently of their origin, their presence and the low average UV radiation field in the post-shocked ISM could account for the changes in the size and charge distribution of the PAH mixture in our ETGs. The short lifetimes of the PAH molecules in such environments and the fact that we see PAH features in the MIR spectra, require either mechanisms to protect the PAHs from destruction by shocks or a continuous supply of carbonaceous material into the ISM.

6. DISCUSSION

Although reminiscent of star-forming galaxies, the PAH spectra seen in our ETGs show remarkable differences to such objects (see items in Section 3.2). In addition, PAH molecules are expected to be destroyed in a few 10^6–10^7 yr in the harsh environment of the ETGs. Hence, the presence of the PAHs in the elliptical galaxies seems to be incompatible with their passive interstellar environments dominated by hot plasma and/or shocks (e.g., Bregman et al. 1992; Micelotta et al. 2010a, 2010b; Panuzzo et al. 2010). So, the key questions to answer are (1) why do we see PAH emission in ETGs, i.e., what is the source of the PAHs in our objects, and (2) why do the PAH spectra present that unusual shape?

There are several possibilities to explain this anomalous emission. We consider them in the following sections.

6.1. Unusual Emission Due to the Presence of an AGN

Smith et al. (2007) noticed that all galaxies of the SINGs sample with peculiar 7.7/11.3 μm inter-band ratios are LINERS, and we also verified that all these galaxies are ETGs. They suggested that the peculiar ratios may be due to the presence of low level AGN activity. In that case, the hard UV radiation field would preferentially destroy small PAH molecules, emitting at shorter wavelengths, and leave unaffected large PAHs, which are thought to emit mainly at $\lambda > 11$ μm. This effect could change the PAH size distribution even at large distances from the center (Voit 1992). Even though this explanation may be correct to some extent, it cannot be the *only* reason for the observed shape of the continuum-subtracted spectra. A significant emission at 6–9 μm could still arise if large PAHs exist in the ionized state (e.g., Bauschlicher et al. 2008, 2009; Boersma et al. 2010). In addition, the source of PAH molecules is unknown in the Smith et al. scenario.

6.2. Emitting Material Recently Accreted

Another possibility has been advanced by Kaneda et al. (2007b, 2008). They suggest that the unusual 7.7/11.3 μm inter-band ratio is due to a recent encounter with a gas-rich galaxy that supplied the ISM with a dust mixture biased toward large, neutral PAHs. A large fraction of neutral PAHs could survive the sputtering effects of the hot ISM because they were originally formed on the mantle of the dust grains. Among their arguments advanced to support this possibility we recall (1) the observed missing anti-correlation between equivalent width (EW) of PAHs and the X-Ray to B-band luminosity ratio, L_X/L_B, implying a lack of relation between the PAH sources (stellar mass-loss rates) and the PAH sinks (X-rays); (2) the observed missing correlation between the 6 μm continuum emission and the PAH (11.3 μm) emission, implying a lack of direct relation between PAH emission and stellar populations of the galaxy; and (3) the correlation between PAH emission and continuum emission around 35 μm, implying a relation between PAH and dust emission. Concerning the first two points, we note that only carbon-rich stars (C stars) can provide carbonaceous material, and that these stars are typical of intermediate age populations. Their presence in an old system like our ETGs would be related to a rejuvenation episode and not to the entire stellar population. One would therefore not expect a correlation between PAH emission and the 6 μm continuum. Furthermore, the EW of PAHs do not depend only on the abundance of carriers but also on the intensity of the exciting radiation, which is mainly UV in the case of the of neutral PAHs (e.g., Tielens 2008). This UV flux can vary from galaxy to galaxy as evidenced by GALEX (e.g., Buson et al. 2009). Finally, we note that point (3) only indicates that there is a common origin for the exciting flux of PAHs and dust.

Another major difficulty faced by this model is that, in many cases, there is no evidence that the last accretion episode was sufficiently recent to allow the carriers to survive destruction by sputtering or shattering mechanisms. Thus, the authors invoke a mechanism that preserves the PAHs in the mantle of dust grains. Apart from these considerations, we note that it remains unexplained why this mixture should be biased toward neutral PAHs, considering that the *accreted material* should be biased toward the ionized PAHs, as is the ISM in normal star-forming galaxies.

6.3. Emitting Material Continuously Supplied by a Population of C Stars

The BF component, up until now, has been observed mainly in carbon-rich pre-planetary nebulae (e.g., Peeters et al. 2002; Sloan et al. 2007). The prototype is IRAS 13416-6243, a carbon star in transition from the AGB phase to the planetary nebula phase. This raises the possibility that a population of such stars is responsible of the BF features observed in ETGs. However, the comparison with our isochrones shows that this cannot be the case because the AGB–PN transition phase is very brief, about two orders of magnitude less than that required to produce the observed features in the integrated spectrum.

Nevertheless, we advance the hypothesis that a population of C stars is the source of freshly synthesized carbonaceous material. In our scheme, amorphous carbon created within the circumstellar envelopes of C-rich stars (e.g., Whittet 1992) is continuously ejected into the ISM and then shocked and exposed to a weak UV radiation field, as described in Section 5.

Such a scenario explains in a more natural way the origin of the emission in these ETGs. In our case, carbonaceous material is *continuously* supplied by the mass-losing carbon stars, whose origin must be a recent rejuvenation episode. The timescale for the process to occur is provided by the age of the carbon star progenitors, which can vary from a few 10^8 yr to a few 10^9 yr, the latter timescale depending on the chemical composition. We thus do not need to advocate a mechanism to preserve these molecules from destruction (for PAHs several 10^7–10^8 yr), as

Kaneda et al. (2008) did, to explain the delay between the actual observation and the epoch of most recent merging or of the gas capture episode. In our model, this delay is simply provided by the stellar evolution clock.

It is interesting to note that such a population of carbon stars should leave a signature in the MIR spectrum of the galaxy, due to the emission of their carbon-rich circumstellar envelopes (Bressan et al. 1998). This emission is similar in shape and peak temperature to the hottest residual continuous component left after the subtraction of the stellar population template. If this is the case, we can make a rough estimate of the number of carbon stars responsible for this emission. Assuming for such stars $L = 10^4\ L_\odot$ and that the light is almost completely reprocessed by an envelope of optical depth $\tau_{1\,\mu m} \sim 10$, we obtain for NGC 5044 ~15,000 C stars. This number would require a rejuvenation episode involving $\sim 1\%$ of the sampled mass of the galaxy, about 1 Gyr ago, which is a typical value found among field galaxies (Longhetti et al. 2000).

In summary, our model can explain both the low 7.7/11.3 μm ratio and the presence of BF families, as well as relax the strong constraint imposed by the sputtering time on the epoch of the gas accretion.

Thus, we argue that the anomalous PAH spectrum is a direct signature of the presence of an intermediate age carbon star population.

7. SUMMARY AND CONCLUSIONS

We have analyzed the MIR spectra of four ETGs characterized by an unusual PAH emission spectrum. These galaxies, which belong to the sample that will be fully presented in Panuzzo et al. (2010), show prominent PAH complexes at 11.3 μm and at 17 μm, with abnormally low 7.7/11.3 μm inter-band ratios.

In contrast to star-forming galaxies, the IRS spectra of our ETGs are dominated by stellar emission at short wavelengths. Thus, in order to investigate their continuum-subtracted spectra, we have first subtracted realistic templates of old stellar populations, derived by high signal-to-noise *Spitzer* observations (Bressan et al. 2006b). After passive stellar template subtraction, we have performed a detailed analysis of the individual dust emission components.

A surprising result is that the 7–9 μm spectral region requires features which are different from those found in normal late-type galaxies, such as those discussed by DL07. In this spectral region, some important features look significantly wider and/or shifted toward longer wavelengths.

With the aim of understanding all the above peculiarities we have analyzed each spectrum by means of dust feature templates (see, e.g., Joblin et al. 2008) and theoretical PAH spectra (see, e.g., Bauschlicher et al. 2008). This method has proved to be very efficient for the understanding of the nature and origin of the PAH emission in Galactic objects, but, to our knowledge, has never been used for external galaxies.

The result of this analysis shows that the ETG spectra are dominated by two main components: (1) the large and neutral PAH component, responsible for the peculiar 7.7/11.3 μm and 6.2/17 μm ratios; and (2) the so-called BF component, which produces the broadening and the shift of the features in the 6–9 μm spectral range. The PAH cations, that are the dominant family in normal galaxies, are almost completely absent in these spectra, indicating that the PAH emitting mixtures in our galaxies have *anomalous* size and charge distributions, biased to large and neutral PAHs. In our sample, the BF components contribute approximately 30%–50% of the total PAH flux between 6 and 14 μm and are responsible for the observed shift and widening of the fitted Drude profiles with respect to DL07. To test whether this result is an artifact of the adopted procedure, we have also analyzed the SINGs H II galaxy NGC 1482 (Smith et al. 2007). In this case, the MIR spectrum is well reproduced by a mixture dominated by cationized PAHs, as is expected in an H II galaxy, while the 8.2 BF contribution is negligible.

Up to now, the BF features have been observed mainly in evolved carbon stars and have been associated with pristine carbonaceous material (e.g., Hony et al. 2001; Peeters et al. 2002; Berné et al. 2007; Sloan et al. 2007; Joblin et al. 2008). Thus, our analysis provides convincing evidence that we are seeing pristine carbonaceous components, still relatively unprocessed by the ISM environment. The most natural explanation we can advance is that this material originates from a population of carbon stars.

We stress that in the above analysis, abandoning the usual blackbody template for the underlying old stellar populations, in favor of a more realistic one derived from passive ETG galaxies, was a fundamental step.

In order to account for the anomalous PAH mixture, we characterized the interstellar radiation fields in our objects by using mid-IR line ratios sensitive to the electron density, gas temperature, and excitation mechanism. The results of this analysis suggest that shock models, with velocities between 100 and 150 km s^{-1}, in a low density ISM, can account for the line ratios observed in our galaxies. If such shocks are present in our objects, they would first destroy the smaller PAHs on timescales of a few 10^8 yr, and would help to maintain the observed size distribution. The extremely low values of the ionization parameter estimated for our objects lead to a predominantly neutral charge distribution.

Present data do not allow us to identify the actual impact of shocks on the dust size distribution, but the peculiar properties of the PAH emission in ETGs may be the result of an environment where the PAH molecules are processed in shocks, and excited by the weak UV radiation field of the old stellar population.

We propose that the unusual PAH spectrum arises from the combination of two effects. First, a rejuvenation episode that recently ceased gives rise to a population of carbon stars that is now *continuously* feeding the ISM with fresh carbonaceous material. From the comparison of the residual warm dust component seen in the galaxies with the circumstellar envelope dust emission of a typical carbon star, we estimate that the rejuvenation fraction is about 1% of the sampled mass. We note that kinematical studies of NGC 5044, NGC 6868, and NGC 7079 show star/gas counterrotation; a strong indication of a past accretion event (see the Appendix). Second, shocks process the ejecta of these carbon stars, destroying smaller PAHs. The weak UV radiation field of an old stellar population excites the processed material, maintains a suitable ratio between neutral and ionized PAHs, and results in the *anomalous* spectral features.

It remains to be clarified whether the presence of these shocks and the occurrence of the rejuvenation episode are causally linked. While there is a general consensus that AGN and star formation activity are linked (see, e.g., Bressan et al. 2002, 2006a), the situation is much less clear for LINERS. However, if our interpretation is correct, our results indicate that LINERS could also have hosted star formation activity in the *recent* past, suggesting a LINER/post-starburst connection.

We are grateful to the anonymous referee, whose comments and suggestions were very useful in improving the manuscript. We acknowledge partial financial support of the Agenzia Spaziale Italiana under contract ASI-INAF I/016/07/0. O.V. acknowledges the hospitality of the INAF-Osservatorio Astronomico di Padova and the financial support of the Mexican Conacyt project 49942-F. This work is based on observations made with the *Spitzer Space Telescope* which is operated by the Jet Propulsion Laboratory, California Institute of Technology, under NASA contract 1407.

APPENDIX

RELEVANT PROPERTIES OF THE GALAXIES SO FAR

The four galaxies considered in this paper belong to the sample of 40 ETGs in low density environments investigated in the mid-infrared by Panuzzo et al. (2010). This sample is biased toward ETGs having emission lines in their optical spectra (see the analysis produced by Rampazzo et al. 2005; Annibali et al. 2006, 2007, 2010). It is known, however, that the presence of ionized gas in ETGs is quite common both in the field as well as in clusters (see, e.g., Macchetto et al. 1996; Sarzi et al. 2005). Most of these ETGs are classified as LINERs using optical diagnostic diagrams (see Annibali et al. 2010).

In the Lick-IDS line-strength indices analysis, performed by Annibali et al. (2007), the four ETGs discussed in this paper were assigned quite different ages.

NGC 1297 is the oldest with a luminosity weighted age of 15.5 ± 1.2 Gyr, but only scant information exists in the literature about this galaxy.

Annibali et al. (2007) attributed to NGC 5044 the very uncertain age of 14.2 ± 10 Gyr. The galaxy, located in a rich group of galaxies (Tully 1988), is rich in dust in the central $10''$ with a clumpy distribution. The ionized gas has a filamentary structure with an extension of about $40''$ (Macchetto et al. 1996). The gas velocity profile is irregular, with many humps and dips, while the inner (within 1/3 of the effective radius) stellar velocity profile is counterrotating with respect to the outer regions (Caon et al. 2000). This galaxy, then, is a very peculiar object, being a possible merger/accretion remnant. Rickes et al. (2004) studied the ionized gas component in NGC 5044 suggesting the presence of both a non-thermal ionization source in the central region and an additional ionization source (possibly hot post-AGB stars) in the outer parts.

NGC 5044 has a set of infrared observations. It has been detected by IRAS and *ISO* (Ferrari et al. 2002, and reference therein). The galaxy belongs to the Kaneda et al. (2008) sample and they detected PAH features and also H_2 rotational emission lines and ionized species using *Spitzer*. Temi et al. (2007) discussed IRAC and MIPS *Spitzer* observations of NGC 5044. They report interstellar emission at 8 μm detected out to 5 kpc as well as 70 μm emission from cold dust exceeding that expected from stellar mass loss. In view of the short sputtering lifetime for extended dust ($\approx 10^7$ yr), they conclude that the extended dust cannot result from a recent merger with a gas-rich galaxy. They support the view that the complex and highly fragmented dust clouds are highly transient and created by stellar mass loss in the central ≈ 1 kpc. The dust clouds are intermittently disrupted and heated by energy released by accretion onto the central black hole (AGN Feedback).

Annibali et al. (2007) provide luminosity weighted ages for NGC 6868 and NGC 7079 being 9.2 ± 1.8 Gyr and 6.7 ± 1.1 Gyr, respectively.

The Fabry–Perot observations of NGC 6868 (Plana et al. 1998) show that the line-of-sight velocity field of the ionized gas component has a velocity amplitude of $\pm$ 150 km s^{-1}. Caon et al. (2000) show that along the axes at P.A. $= 30^\circ$ and 70° the gas and stars have similar kinematical properties, but along P.A. $= 120^\circ$ the gas counterrotates with respect to the stellar component. Zeilinger et al. (1996) noticed the presence of an additional inner gas component which they suggested could be due to the superposition of the two unresolved counterrotating components, one dominating the inner region, the other dominating the outer parts. Stars also show a kinematically decoupled counterrotating core. The stellar velocity dispersion decreases toward the galaxy center. The above kinematics suggest that NGC 6868 could have had a recent accretion episode which could explain the relatively low-luminosity weighted age.

Bettoni & Galletta (1997) found that in NGC 7079 the gas is rotating in a direction opposite to that of the stars (gas counterrotation).

We may conclude that according to the current interpretation of the peculiar gas versus stellar kinematics found in NGC 5044, NGC 6868, and NGC 7079, accretion/merging events could have occurred in these galaxies.

Both NGC 6868 and NGC 7079 have been observed in CO. Huchtmeier & Tammann (1992) observed with the SEST NGC 6868 and provide a CO upper limit. Assuming this value we obtain an upper limit to the cold H_2 mass of $2.0 \times 10^8\ M_\odot$ (adopting a galactic X factor $X_{CO} = 4.6\ M_\odot$ (K km s^{-1} pc^2)$^{-1}$; see Solomon et al. 1987). For NGC 7079, Bettoni et al. (2001) estimated a mass of cold H_2 of $8.82 \times 10^7\ M_\odot$ within the central 2 kpc radius.

In Table A.1, we collect relevant properties of the galaxies. Column 1 gives the name of the galaxy; Column 2 the morphological type; Column 3 the class of activity; Columns 4, 5, and 6 the luminosity weighted age and the metallicity and α-enhancement computed from optical spectra by Annibali et al.

Table A.1
General Properties of the Sample

NGC	Type	Activity Class	Age (Gyr)	Z	[α/Fe]	M^c_{H2} ($M_\odot$)	log L_X (erg s^{-1})	D (Mpc)
1297	SAB0 pec:	LINER	15.5 ± 1.2	0.012 ± 0.001	0.29 ± 0.04			19.8
5044	E0	LINER	14.2 ± 10.0	0.015 ± 0.022	0.34 ± 0.17		42.74	42.8
6868	E2	LINER	9.2 ± 1.8	0.033 ± 0.006	0.19 ± 0.03	$< 2.0 \times 10^8$	41.23	37.5
7079	SB0	LINER	6.7 ± 1.1	0.016 ± 0.003	0.21 ± 0.05	8.82×10^7		34.2

Notes. Column 2: morphological types are derived from RC3; Column 3: activity class from Annibali et al. (2010); Columns 4–6 from Annibali et al. (2007); Column 7: H_2 content from Huchtmeier & Tammann (1992) and Bettoni et al. (2001) for NGC 6868 and NGC 7079, respectively; Column 8: X-ray Luminosity from Ogle et al. (2006); Column 9: distances adopted are derived from NED.

(2007). Column 7 lists the molecular masses obtained from CO observations and by using the galactic X-factor. Column 8 displays the X-ray luminosity reported in O'Sullivan et al. (2001). In Column 9, we give the luminosity distance taken from the NASA/IPAC Extragalactic Database (NED) using $H_0 = 73$ km s^{-1} Mpc^{-1}.

REFERENCES

Allamandola, L. J., Hudgins, D. M., & Sandford, S. A. 1999, ApJ, 511, L115
Allamandola, L. J., Tielens, A. G. G. M., & Barker, J. R. 1989, ApJS, 71, 733
Allen, M. G., Groves, B. A., Dopita, M. A., Sutherland, R. S., & Kewley, L. J. 2008, ApJS, 178, 20
Annibali, F., Bressan, A., Rampazzo, R., Danese, L., & Zeilinger, W. W. 2007, A&A, 463, 455
Annibali, F., Bressan, A., Rampazzo, R., & Zeilinger, W. W. 2006, A&A, 445, 79
Annibali, F., Bressan, A., Rampazzo, R., Zeilinger, W. W., Vega, O., & Panuzzo, P. 2010, A&A, in press (arXiv:1004.1647)
Bakes, E. L. O., Tielens, A. G. G. M., & Bauschlicher, C. W., Jr. 2001, ApJ, 556, 501
Bauschlicher, C. W., Jr. 2002, ApJ, 564, 782
Bauschlicher, C. W., Jr., Peeters, E., & Allamandola, L. J. 2008, ApJ, 678, 316
Bauschlicher, C. W., Jr., Peeters, E., & Allamandola, L. J. 2009, ApJ, 697, 311
Berné, O., Joblin, C., Fuente, A., & Ménard, F. 2009, A&A, 495, 827
Berné, O., et al. 2007, A&A, 469, 575
Bettoni, D., & Galletta, G. 1997, A&AS, 124, 61
Bettoni, D., Galletta, G., Garcia-Burillo, S., & Rodriguez-Franco, A. 2001, A&A, 374, 421
Boersma, C., Bauschlicher, C. W., Allamandola, L. J., Ricca, A., Peeters, E., & Tielens, A. G. G. M. 2010, A&A, 511, A32
Boselli, A., et al. 2005, ApJ, 629, L29
Bouwman, J., et al. 2008, ApJ, 683, 479
Bregman, J. D., Bregman, J. N., & Temi, P. 2008, in ASP Conf. Ser. 381, Infrared Diagnostics of Galaxy Evolution, ed. R.-R. Chary, H. I. Teplitz, & K. Sheth (San Francisco, CA: ASP), 34
Bregman, J. N., Hogg, D. E., & Roberts, M. S. 1992, ApJ, 387, 484
Bregman, J. N., & Parriott, J. R. 2009, ApJ, 699, 923
Bressan, A., Della Valle, M., & Marziani, P. 2002, MNRAS, 331, L25
Bressan, A., Falomo, R., Valdés, J. R., & Rampazzo, R. 2006a, ApJ, 645, L101
Bressan, A., Granato, G. L., & Silva, L. 1998, A&A, 332, 135
Bressan, A., et al. 2006b, ApJ, 639, L55
Buson, L. M., et al. 2009, ApJ, 705, 356
Buss, R. H., Jr., Tielens, A. G. G. M., Cohen, M., Werner, M. W., Bregman, J. D., & Witteborn, F. C. 1993, ApJ, 415, 250
Caon, N., Macchetto, D., & Pastoriza, M. 2000, ApJS, 127, 39
Cesarsky, D., Lequeux, J., Ryter, C., & Gérin, M. 2000, A&A, 354, L87
Chiar, J. E., Tielens, A. G. G. M., Whittet, D. C. B., Schutte, W. A., Boogert, A. C. A., Lutz, D., van Dishoeck, E. F., & Bernstein, M. P. 2000, ApJ, 537, 749
Clemens, M. S., et al. 2010, A&A, 518, L50
Dale, D. A., et al. 2006, ApJ, 646, 161
Dopita, M. A., Koratkar, A. P., Allen, M. G., Tsvetanov, Z. I., Ford, H. C., Bicknell, G. V., & Sutherland, R. S. 1997, ApJ, 490, 202
Draine, B. T., & Li, A. 2007, ApJ, 657, 810
Dwek, E., & Arendt, R. G. 1992, ARA&A, 30, 11
Elson, R. A. W., Fall, S. M., & Freeman, K. C. 1987, ApJ, 323, 54
Ferrari, F., Pastoriza, M. G., & Macchetto, F. D. 2002, A&A, 389, 355
Ferrari, F., Pastoriza, M. G., Macchetto, F., & Caon, N. 1999, A&AS, 136, 269
Flagey, N., Boulanger, F., Verstraete, L., Miville Deschênes, M. A., Noriega Crespo, A., & Reach, W. T. 2006, A&A, 453, 969
Förster Schreiber, N. M., Roussel, H., Sauvage, M., & Charmandaris, V. 2004, A&A, 419, 501
Galliano, F., Madden, S. C., Tielens, A. G. G. M., Peeters, E., & Jones, A. P. 2008, ApJ, 679, 310
Goto, M., et al. 2003, ApJ, 589, 419
Hony, S., Van Kerckhoven, C., Peeters, E., Tielens, A. G. G. M., Hudgins, D. M., & Allamandola, L. J. 2001, A&A, 370, 1030
Hrivnak, B. J., Volk, K., & Kwok, S. 2000, ApJ, 535, 275
Huchtmeier, W. K., & Tammann, G. A. 1992, A&A, 257, 455
Joblin, C., Berné, O., Simon, A., & Mulas, G. 2009, in ASP Conf. Ser. 414, Cosmic Dust—Near and Far, ed. T. Henning, E. Grun, & J. Steinacker (San Francisco, CA: ASP), 383
Joblin, C., Szczerba, R., Berné, O., & Szyszka, C. 2008, A&A, 490, 189
Kaneda, H., Onaka, T., & Sakon, I. 2005, ApJ, 632, 83
Kaneda, H., Onaka, T., & Sakon, I. 2007a, ApJ, 666, L21
Kaneda, H., Onaka, T., & Sakon, I. 2007b, PASJ, 666, L21
Kaneda, H., Onaka, T., Sakon, I., Kitayama, T., Okada, Y., & Suzuki, T. 2008, ApJ, 684, 270
Kennicutt, R. C., Jr., et al. 2003, PASP, 115, 928
Kim, H. S., & Saykally, R. J. 2002, ApJS, 143, 455
Knapp, G. R., Guhathakurta, P., Kim, D.-W., & Jura, M. A. 1989, ApJS, 70, 329
Kraemer, K. E., Sloan, G. C., Bernard-Salas, J., Price, S. D., Egan, M. P., & Wood, P. R. 2006, ApJ, 652, L25
Kwok, S., & Hrivnak, B. J. 1989, in Infrared Spectroscopy in Astronomy, Vol. 290 (Noordwijk: ESA), 363
Leger, A., D'Hendecourt, L., Boissel, P., & Desert, F. X. 1989, A&A, 213, 351
Li, A., & Draine, B. T. 2001, ApJ, 554, 778
Longhetti, M., Bressan, A., Chiosi, C., & Rampazzo, R. 2000, A&A, 353, 917
Macchetto, F., Pastoriza, M., Caon, N., Sparks, W. B., Giavalisco, M., Bender, R., & Capaccioli, M. 1996, A&AS, 120, 463
Marino, A., Rampazzo, R., Bianchi, L., Annibali, F. B., Buson, L. M., Clemens, M. S., Panuzzo, P., & Zeilinger, W. W. 2010, MNRAS, submitted
Mathis, J. S., Mezger, P. G., & Panagia, N. 1983, A&A, 128, 212
Micelotta, E. R., Jones, A. P., & Tielens, A. G. G. M. 2010a, A&A, 510, A37
Micelotta, E. R., Jones, A. P., & Tielens, A. G. G. M. 2010b, A&A, 510, A36
Morganti, R., et al. 2006, MNRAS, 371, 157
Nagar, N. M., Falcke, H., & Wilson, A. S. 2005, A&A, 435, 521
Ogle, P., Antonucci, R., Appleton, P. N., & Whysong, D. 2006, ApJ, 668, 699
O'Sullivan, E., Forbes, D. A., & Ponman, T. J. 2001, MNRAS, 328, 461
Panuzzo, P., Rampazzo, R., Bressan, A., Vega, O., Annibali, F., Buson, L. M., Clemens, M., & Zeilinger, W. W. 2010, A&A, submitted
Panuzzo, P., et al. 2007, ApJ, 656, 206
Peeters, E., Hony, S., VanKerckhoven, C., Tielens, A. G. G. M., Allamandola, L. J., Hudgins, D. M., & Bauschlicher, C. W. 2002, A&A, 390, 1089
Peeters, E., Spoon, H. W. W., & Tielens, A. G. G. M. 2004, ApJ, 613, 986
Plana, H., Boulesteix, J., Amram, Ph., Carignan, C., & Mendes de Oliveira, C. 1998, A&AS, 128, 75
Puget, J. L., & Leger, A. 1989, ARA&A, 27, 161
Rampazzo, R., Annibali, F., Bressan, A., Longhetti, M., Padoan, F., & Zeilinger, W. W. 2005, A&A, 433, 497
Rapacioli, M., Calvo, F., Joblin, C., Parneix, P., Toublanc, D., & Spiegelman, F. 2006, A&A, 460, 519
Rapacioli, M., Joblin, C., & Boissel, P. 2005, A&A, 429, 193
Renzini, A. 2007, in ASP Conf. Ser. 380, At the Edge of the Universe: Latest Results from the Deepest Astronomical Surveys, ed. J. Afonso et al. (San Francisco, CA: ASP), 309
Rickes, M. G., Pastoriza, M. G., & Bonatto, Ch. 2004, A&A, 419, 449
Roussel, H., Sauvage, M., Vigroux, L., & Bosma, A. 2001, A&A, 372, 427
Sarzi, M., Rix, H. W., Shields, J. C., Ho, L. C., Barth, A. J., Rudnick, G., Filippenko, A. V., & Sargent, W. L. W. 2005, ApJ, 628, 169
Schutte, W. A., Tielens, A. G. G. M., & Allamandola, L. J. 1993, ApJ, 415, 397
Schutte, W. A., Tielens, A. G. G. M., Allamandola, L. J., Wooden, D. H., & Cohen, M. 1990, ApJ, 360, 577
Sloan, G. C., et al. 2005, ApJ, 632, 956
Sloan, G. C., et al. 2007, ApJ, 664, 1144
Smith, J. D. T., et al. 2007, ApJ, 656, 770
Solomon, P. M., Rivolo, A. R., Barrett, J., & Yahil, A. 1987, ApJ, 319, 730
Szczerba, R., Siódmiak, N., & Szyszka, C. 2005, in AIP Conf. Proc. 804, Planetary Nebulae as Astronomical Tools, ed. R. Szczerba, G. Stasinska, & S. K. Górny (Melville, NY: AIP), 214
Temi, P., Brighenti, F., & Mathews, W. G. 2007, ApJ, 666, 222
Temi, P., Brighenti, F., Mathews, W. G., & Bregman, J. D. 2004, ApJS, 151, 237
Tielens, A. G. G. M. 2008, ARA&A, 46, 289
Tielens, A. G. G. M. 2005, The Physics and Chemistry of the Interstellar Medium (Cambridge: Cambridge Univ. Press)
Tully, R. B. 1988, Science, 242, 310
Turner, J., Kirby-Docken, K., & Dalgarno, A. 1977, ApJS, 35, 281
van Diedenhoven, B., Peeters, E., Van Kerckhoven, C., Hony, S., Hudgins, D. M., Allamandola, L. J., & Tielens, A. G. G. M. 2004, ApJ, 611, 928
Vega, O., Silva, L., Panuzzo, P., Bressan, A., Granato, G. L., & Chavez, M. 2005, MNRAS, 364, 1286
Verhoelst, T., van der Zypen, N., Hony, S., Decin, L., Cami, J., & Eriksson, K. 2009, A&A, 498, 127
Voit, G. M. 1992, MNRAS, 258, 841
Whittet, D. C. B. 1992, Dust in the Galactic Environment (Bristol: Institute of Physics Publishing)
Xilouris, E. M., Madden, S. C., Galliano, F., Vigroux, L., & Sauvage, M. 2004, A&A, 416, 41
Zeilinger, W. W., et al. 1996, A&AS, 120, 257